

1 **Structural and kinetic analysis of the COP9-Signalosome activation and the**
2 **cullin-RING ubiquitin ligase deneddylation cycle**

3 Ruzbeh Mosadeghi^{1,2,*}, Kurt M. Reichermeier², Martin Winkler³, Anne Schreiber³, Justin M.
4 Reitsma², Yaru Zhang², Florian Stengel^{4,8}, Junyue Cao², Minsoo Kim², Michael J. Sweredoski⁵, Sonja
5 Hess⁵, Alexander Leitner^{4,8}, Ruedi Aebersold^{4,6}, Matthias Peter^{3,&}, Raymond J. Deshaies^{2,7,&} and
6 Radoslav I. Enchev^{3,*,&}

7 ¹ Keck School of Medicine of the University of Southern California/California Institute of
8 Technology Combined MD/PhD Program

9 ² Division of Biology and Biological Engineering, California Institute of Technology, Pasadena CA,
10 USA, 911250

11 ³ Department of Biology, Institute of Biochemistry, Swiss Federal Institute of Technology, Otto-
12 Stern Weg 3, 8093 Zurich, Switzerland

13 ⁴ Department of Biology, Institute of Molecular Systems Biology, Swiss Federal Institute of
14 Technology, HPT E 78, August-Piccard-Hof 1, 8093 Zürich, Switzerland

15

16 ⁵ Proteome Exploration Lab, Beckman Institute, California Institute of Technology, Pasadena CA,
17 USA, 91125

18 ⁶ Faculty of Science, University of Zurich, Zurich, Switzerland

19 ⁷ Howard Hughes Medical Institute

20

21 ⁸ Current Address - Department of Biology, University of Konstanz, 78457 Konstanz, Germany

22

23 * equal contribution

24 & corresponding authors

25 **Competing Interests Statement: The authors declare no competing interests**

26

27 **Abstract**

28 The COP9-Signalosome (CSN) regulates cullin–RING ubiquitin ligase (CRL) activity and assembly
29 by cleaving Nedd8 from cullins. Free CSN is autoinhibited, and it remains unclear how it becomes
30 activated. We combine structural and kinetic analyses to identify mechanisms that contribute to
31 CSN activation and Nedd8 deconjugation. Both CSN and neddylated substrate undergo large
32 conformational changes upon binding, with important roles played by the N-terminal domains of
33 Csn2 and Csn4 and the RING domain of Rbx1 in enabling formation of a high affinity, fully active
34 complex. The RING domain is crucial for deneddylation, and works in part through conformational
35 changes involving insert-2 of Csn6. Nedd8 deconjugation and re-engagement of the active site zinc
36 by the autoinhibitory Csn5 glutamate-104 diminish affinity for Cul1/Rbx1 by ~100-fold, resulting
37 in its rapid ejection from the active site. Together, these mechanisms enable a dynamic
38 deneddylation-disassembly cycle that promotes rapid remodeling of the cellular CRL network.

39 **Introduction**

40 Cullin–RING ubiquitin ligases comprise one of the largest families of regulatory enzymes in
41 eukaryotic cells (Deshaies and Joazeiro, 2009). With as many as 240 different enzyme complexes,
42 these E3s control a broad array of biological processes (Skaar et al., 2013). CRLs comprise seven
43 distinct cullin–RING cores, each of which interacts with its own dedicated set of adaptor–substrate
44 receptor complexes. Although ubiquitination by CRL enzymes is often regulated by covalent
45 modifications of the substrate that stimulate binding to the substrate receptor, the CRL enzymes
46 themselves are also subject to regulation.

47 A key mechanism that controls the activity of all known CRLs is the conjugation of the
48 ubiquitin-like protein Nedd8 to a conserved lysine residue in the cullin subunit (e.g. K720 in
49 human Cul1)(Enchev et al., 2015). The available structural and biochemical data indicate that
50 Nedd8 conjugation (neddylation) stabilizes a profound conformational change in the C-terminal
51 domain of the cullin. It loosens the interaction of the WHB domain with the RING subunit, allowing
52 both of them to sample a greater conformational space (Duda et al., 2008), thereby enhancing the
53 ability of the RING domain to promote ubiquitin transfer to substrate (Duda et al., 2008; Saha and
54 Deshaies, 2008; Yamoah et al., 2008).

55 In addition to direct effects on ubiquitin ligase activity, Nedd8 also protects Skp1/Cul1/F-
56 box (SCF) complexes from the substrate receptor exchange factor (SREF) Cand1 (Pierce et al.,

57 2013; Schmidt et al., 2009; Wu et al., 2013; Zemla et al., 2013). Cand1 binds unmodified SCF
58 complexes and promotes rapid dissociation of the F-box protein (FBP)/Skp1 substrate receptor-
59 adaptor module from the Cul1/Rbx1 core. Cand1 can subsequently be dissociated from Cul1 by a
60 different FBP/Skp1 complex, and as a result Cand1 functions as an SREF that accelerates the rate
61 at which Cul1/Rbx1 comes to equilibrium with different FBP/Skp1 substrate receptor-adaptor
62 complexes (Pierce et al., 2013). Importantly, the SREF activity of Cand1 is tightly restricted by
63 Nedd8. Cand1 is not able to bind stably to Cul1 and promote dissociation of FBP/Skp1 when Cul1
64 is conjugated to Nedd8 (Liu et al., 2002; Pierce et al., 2013). These observations underscore the
65 importance of neddylation not only for controlling the enzymatic activity of CRLs, but also
66 potentially for controlling the repertoire of assembled CRLs.

67 The key role of Nedd8 in CRL biology highlights the importance of the enzymatic pathways
68 that attach and remove Nedd8 (Enchev et al., 2015). Of particular significance is the rate of Nedd8
69 deconjugation, because it serves as the gateway for the exchange cycle; once Nedd8 is removed, a
70 CRL complex is susceptible to the potent SREF activity of Cand1, and its substrate receptor can be
71 exchanged (Pierce et al., 2013). Deconjugation of Nedd8 is mediated by the COP9-signalosome
72 (CSN), which is an eight-subunit Nedd8 isopeptidase (Lyapina et al., 2001). The enzymatic activity
73 of CSN resides in its Csn5 subunit, which contains a metalloprotease active site referred to as the
74 'JAMM' domain (Cope et al., 2002). The JAMM domain has the general structure E₇₆-X_n-H₁₃₈-X-
75 H₁₄₀-X₁₀-D₁₅₁ (the subscripts refer to the sequence position of these residues in human Csn5),
76 wherein the H and D residues coordinate a zinc ion. The fourth zinc-coordination site is occupied
77 by a water molecule that also forms a hydrogen bond to E76 (Ambroggio et al., 2004; Sato et
78 al., 2008; Tran et al., 2003). Deneddylation of CRLs by CSN is rapid but can be regulated by CRL
79 substrates (Emberley et al., 2012; Enchev et al., 2012; Fischer et al., 2011). Structural analysis
80 suggests that a CRL ubiquitination substrate bound to a substrate receptor sterically prevents
81 concurrent binding of CSN (Enchev et al., 2012; Fischer et al., 2011). This suggests a model
82 wherein a CRL complex has a higher probability of being conjugated to Nedd8 (and therefore of
83 being shielded from Cand1) as long as it is bound to substrate. Upon dissociation of substrate, a
84 race ensues between binding of either a new substrate or CSN. If CSN wins, Nedd8 is removed,
85 paving the way for Cand1 to initiate substrate receptor exchange.

86 Recently, a crystal structure of free CSN was determined (Lingaraju et al., 2014). A major
87 insight to emerge from the structure was the unexpected finding that Csn5 was present in an

88 autoinhibited state, wherein a glutamate (Csn5-E104) within the ‘insert-1’ (INS1) sequence
89 common to JAMM family members (Sato et al., 2008) forms a fourth ligand to the zinc, displacing
90 the catalytic Csn5-E76-bound water molecule and shifting Csn5-E76. Csn5-E104 is found in all
91 Csn5 orthologs, but not in other JAMM proteins, suggesting that this mode of regulation is
92 conserved but unique to CSN. Comparison of the structure of free CSN to the structure of a
93 catalytically-dead mutant CSN bound to Nedd8-conjugated SCF^{Skp2} determined by negative stain
94 electron microscopy (Enchev et al., 2012) implied that binding of substrate to CSN may induce
95 several conformational changes in the latter, including movement of the N-terminal domains
96 (NTD) of Csn2 and Csn4 towards the cullin. The latter movement, in turn, might be further
97 propagated to the Csn5/6 module (Lingaraju et al., 2014). Moreover, it is reasonable to expect that
98 during catalysis INS1 moves out of the active site and Csn5-E76 adopts a position similar to that
99 observed in a crystallographic structure of Csn5 in isolation (Echalier et al., 2013). Interestingly, if
100 Csn5-E104 is mutated to an alanine, CSN more rapidly cleaves the simple model substrate
101 ubiquitin-rhodamine (Lingaraju et al., 2014). This was interpreted to mean that the primary
102 reason for the autoinhibited state is to keep CSN off until it binds a physiologic substrate, which
103 would prevent spurious cleavage of non-cullin Nedd8 conjugates and possibly even ubiquitin
104 conjugates. However, the full extent of the conformational changes required to form an activated
105 complex between CSN and its neddylated substrate, as well as the detailed molecular basis for
106 these changes remain to be established. Therefore, at present, the mechanism of how CSN is
107 switched on and off and the significance of this switching behavior remain unknown.

108 **Results**

109 **Structural insights from cryo EM and single particle analysis of a CSN-SCF-Nedd8^{Skp2/Cks1}** 110 **complex**

111 To gain detailed insights into the molecular determinants underlying activation of CSN, we
112 performed cryo electron microscopy (cryo EM) and single particle analysis of CSN^{5H138A} (we use
113 the nomenclature CSN^{#x} where # refers to subunit number and x to the specific mutation) in
114 complex with neddylated SCF^{Skp2/Cks1} (the sample is described in (Enchev et al., 2012) (Figure 1A,
115 Figure 1-figure supplements 1A-D). The Csn5-H138A mutant lacks one of the JAMM ligands that
116 coordinate the catalytic zinc. This mutant forms a normal CSN complex that has been extensively
117 characterized (Enchev et al., 2012). We used ~75000 single molecular images for the final three-
118 dimensional reconstruction and the structure was refined to a nominal resolution of 7.2 Å,

119 according to the ‘gold standard’ criterion of a Fourier shell correlation (FSC) of 0.143 (Rosenthal
120 and Henderson, 2003; Scheres and Chen, 2012) (Figure 1–figure supplements 1C–D). However,
121 some regions in the density map were better defined than others (see below). To avoid over-
122 interpretation, for the subsequent analysis we low-pass filtered the map to 8.5 Å, according to the
123 more stringent criterion of an FSC of 0.5.

124 The cryo EM structure reported here, alongside the available crystal structure of CSN
125 (Lingaraju et al., 2014), enabled us to visualize a broad array of conformational changes that take
126 place upon complex formation in both CSN and neddylated Cul1/Rbx1, well beyond what was
127 possible with the prior lower resolution model based on negative stain EM (Figure 1). Specifically,
128 this allowed us to describe movements of the N-terminal domains of Csn2 and Csn4, the MPN
129 domains of Csn5 and Csn6. Moreover, in contrast to our previous work, we could locate the RING
130 domain of Rbx1, as well as Nedd8 and the winged-helix B (WHB) domain of Cul1 relative to Csn5.
131 Nevertheless, the present resolution precludes the determination of the exact orientations of the
132 latter domains but notably, the relative positions of the RING, WHB and Nedd8 reported here have
133 not been reported in any structural model of a cullin, and strongly suggest that both the enzyme
134 and substrate undergo significant conformational rearrangements to enable catalysis.

135 To obtain the model shown in Figure 1, we initially docked the crystal structure of CSN
136 (Lingaraju et al., 2014) and a model of Cul1-Nedd8/Rbx1/Skp1/Skp2/Cks1 (Enchev et al., 2012)
137 as rigid bodies into the electron density map (Figure 1–figure supplements 1E–H). We observed
138 very good matches between the respective map segments and the atomic coordinates for the
139 scaffold subunits Csn1, Csn3, Csn7 and Csn8, the winged-helix domains of Csn2 and Csn4 (Figure
140 1–figure supplement 1E), and the helical bundle formed by the C-termini of all eight CSN subunits
141 (Figure 1–figure supplement 1F) as well as the expected recovery of secondary structure at this
142 resolution. Similarly, there was a very good overlap between the coordinates of Cul1 (with the
143 exception of helix29 and the WHB domain, see below) and Skp1 and the corresponding electron
144 density segments (Figure 1–figure supplement 1G). However, the local resolution was lower
145 without recovery of secondary structure in the N-terminal domain of Cul1. Moreover, the density
146 of the substrate receptor Skp2/Cks1 was poorly defined (Figure 1–figure supplement 1G),
147 indicating a potential flexibility in this region. Since the presence of Skp1/Skp2 had modest effects
148 on the affinity and deneddylation activity (see below), we did not interpret this observation
149 further.

150 In contrast to the large segments of CSN that were unaltered upon binding substrate, there
151 was nearly no overlap between the EM density map and the N-terminal portions of Csn2 and Csn4,
152 as well as the MPN-domains of Csn5 and Csn6, the RING domain of Rbx1, the WHB domain of Cul1,
153 and Nedd8 (Figure 1–figure supplement 1H). We thus docked these domains individually (Figure
154 1B, Movie 1). A Csn2 N-terminal fragment encompassing the portion between its
155 crystallographically resolved N-terminus (amino acid 30) through to a flexible loop at amino acid
156 180, was docked as a rigid body (Figure 1–figure supplement 1I), positioning it close to the four-
157 helical bundle and helix 24 of Cul1 (Zheng et al., 2002). An N-terminal fragment of Csn4, spanning
158 amino acids 1 to 295, which ends in a previously reported hinge loop (Lingaraju et al., 2014), was
159 also docked independently as a rigid body (Figure 1–figure supplement 1J). The resulting
160 conformation of Csn4 resembles a crystal form of Csn4 observed in isolation (Lingaraju et al.,
161 2014). The two N-terminal helical repeat motifs of Csn4 make contacts with the winged-helix A
162 domain of Cul1 (Figure 1B and Figure 1–figure supplement 1J, right hand panel, red arrow and
163 green circle). Moreover, these positions of Csn2 and Csn4 delineated a density in the map, which
164 could accommodate the RING domain of Rbx1 (Figure 1B and Figure 1–figure supplement 1J, right
165 hand panel, black ellipse), with the RING proximal to two conserved helices between amino acids
166 160 and 197 of Csn4 (Figures 1B and Figure 1–figure supplement 1K, black arrow) and a loop in
167 Csn2 located between residues 289 and 306. The exact orientation of the RING domain awaits a
168 structure at higher resolution.

169 To improve the fit of Csn5 and Csn6, we moved their MPN domains as rigid bodies into the
170 neighboring map segment of similar shape and dimensions (Figure 1–figure supplement 1L). The
171 local resolution in this region was lower, presumably due to higher flexibility around the catalytic
172 site. Importantly, after docking Csn5, we observed two empty neighboring densities (Figure 1–
173 figure supplement 1L, right hand panel, circles), which accommodated the two yet undocked
174 protein components – Nedd8 and the WHB domain of Cul1 (Figure 1–figure supplement 1M). The
175 docking of the latter was enabled by allowing helix 29 and the WHB, amino acids 690 to the C-
176 terminus of Cul1, to move as a rigid body towards Csn5. However, we did not observe an electron
177 density around helix 29 of Cul1, consistent with a structural flexibility in this region. This model
178 places the neddylated WHB domain in close binding proximity to the RING domain, as well as both
179 INS1 and INS2 of Csn5. The hydrophobic patch of Nedd8 is facing INS1, and not the WHB domain,
180 as has been reported for the isolated neddylated C-terminal domain of Cul5 (Duda et al 2008).
181 Similar to the RING domain, we cannot be fully certain about the exact orientations of Nedd8 and

182 the WHB domain at the present resolution. Nevertheless, to further substantiate this docking, we
183 mutagenized conserved charged residues in the INS2 domain of Csn5 as well as the WHB domain,
184 and as expected all of these constructs showed reduced catalytic activity in deneddylation assays
185 (Figure 1–figure supplement 1N, O).

186 We sought orthogonal experimental validation for the molecular docking of the individual
187 subunits and domains in the electron density map by performing cross-linking coupled to mass
188 spectrometric analysis of the cross-linked peptides (Leitner et al., 2014) following the procedure
189 described in Birol et al. (2014) (supplementary files 1-6). For the cross-linker used in this study
190 (disuccinimidylsuberate H₁₂/D₁₂), the maximum predicted distance between two cross-linked
191 lysine residues is generally accepted to be below ~ 30 Å (Politis et al., 2014). As shown in
192 supplementary files 1, out of the 39 high-confidence inter-subunit cross-links detected within the
193 CSN^{5H138A}-N8-SCF^{Skp2/Cks1} complex at a false discovery rate (FDR) of 5 percent, the great majority
194 was within regions of modeled atomic structure and only six links exhibited a distance larger than
195 30 Å when mapped onto our model. However, all of these larger-distance links are connected to
196 the flexibly positioned Skp2 density. Moreover, we further performed similar cross-linking
197 experiments on a number of different CSN-CRL complexes, varying the substrate receptor, the
198 cullin and the neddylation state (supplementary files 2-6). All results were consistent with the
199 architecture proposed here for CSN^{5H138A}-N8-SCF^{Skp2/Cks1}. Intriguingly, when taking into account
200 cross-links with an FDR of up to 0.25 (supplementary files 2 and 3), we found two cross-links that
201 support proximity of K290 in Csn4 and K89 in the RING domain (supplementary file 2), as well as
202 K32 in Csn4-NTD and K587 in Cul1, which is in the immediate vicinity of the WHA domain of Cul1
203 (supplementary file 3), as suggested by our EM reconstruction.

204 **Development and validation of an assay to measure binding of CSN to substrate and** 205 **product.**

206 To understand how the structure of CSN and the CSN–SCF complex relates to substrate
207 binding and the mechanism of deneddylation, we sought to develop quantitative binding assays to
208 measure interaction of CSN with its substrates and products. To this end, the environmentally-
209 sensitive dye dansyl was conjugated to the C-terminus of Cul1 using ‘sortagging’ (Theile et al.,
210 2013) to generate dansylated Cul1/Rbx1 (Cul1^d/Rbx1)(Figure 2–figure supplement 2A).
211 Cul1^d/Rbx1 exhibited normal E3 activity (Figure 2–figure supplement 2B) and bound CSN with an
212 affinity similar to Cul1/Rbx1 based on their IC₅₀ values for competitive inhibition of a

213 deneddylation reaction (Figure 2–figure supplement 2C; Emberley et al., 2012). When Cul1^d/Rbx1
214 was incubated with CSN (all CSN preparations used in this work are shown in Figure 2–figure
215 supplement 2D), we observed an increase in dansyl fluorescence (Figure 2A). This signal was due
216 to specific binding because it was chased upon addition of excess unlabeled Cul1/Rbx1 (Figure 2A,
217 titration shown in Figure 2–figure supplement 2E) or Cand1 (Figure 2–figure supplement 2F),
218 which competes for substrate deneddylation by CSN (Emberley et al., 2012; Enchev et al., 2012).
219 Thus, we concluded that the increase in dansyl fluorescence accurately reported on the interaction
220 of CSN with Cul1^d/Rbx1. Using this assay we determined that CSN bound Cul1^d/Rbx1 with a K_d of
221 310 nM (Figure 2B). Cul1^d/Rbx1 binding to CSN was only modestly affected by the addition of free
222 Nedd8 (Figure 2–figure supplement 2G) or assembly with Skp2/Skp1 (Figure 2–figure
223 supplement 2H) or Fbxw7/Skp1 (Figure 2–figure supplement 2I).

224 We next sought to measure binding of neddylated Cul1^d/Rbx1 (Cul1^d-N8/Rbx1) to CSN but
225 it was not possible because the substrate was rapidly deneddylated. To circumvent this problem,
226 we performed binding assays with the extensively characterized inactive mutant CSN^{5H138A} (assay
227 confirming loss of activity is shown in Figure 3–figure supplement 3A). Remarkably, CSN^{5H138A}
228 bound Cul1^d-N8/Rbx1 ~200-fold more tightly than CSN bound Cul1^d/Rbx1 (K_d 1.6 nM vs. 310 nM;
229 Figures 3A–B). Note that the estimated K_d falls well below the fixed concentration of Cul1^d-
230 N8/Rbx1 used in the assay. This introduces greater uncertainty into our estimate but nevertheless
231 we can conclude with confidence that the binding of substrate to CSN^{5H138A} is very tight (≤ 5 nM;
232 see Materials and Methods for further discussion of this matter). As reported above for CSN
233 binding to product, addition of Skp2/Skp1 or Fbxw7/Skp1 had comparatively minor effects on
234 affinity (Figure 3–figure supplements 3B–C). Thus, for the sake of simplicity, we used Cul1^d/Rbx1
235 heterodimer for the remaining binding experiments.

236 The strikingly high affinity we observed for binding of CSN^{5H138A} to Cul1^d-N8/Rbx1 led us to
237 question whether it was mainly due to Nedd8 or whether the H138A mutation might also enhance
238 affinity. To this end, we measured binding of CSN^{5H138A} to Cul1^d/Rbx1 and observed an
239 unexpectedly low K_d of ~10 nM (Figure 3B, Figure 3–figure supplement 3D), which was confirmed
240 with an independent preparation of CSN^{5H138A} (Figure 3–figure supplement 3E). Thus, neddylation
241 improved affinity of Cul1^d/Rbx1 for CSN^{5H138A} by ~6-fold, whereas the Csn5-H138A mutation
242 improved affinity for Cul1^d/Rbx1 by ~30-fold. The high affinity binding of CSN^{5H138A} to substrate
243 was supported by an orthogonal competition experiment in which 100 nM CSN^{5H138A} completely

244 blocked deneddylation of 75 nM Cul1-N8/Rbx1 (Figure 3–figure supplement 3A). We considered
245 the possibility that the Csn5-H138A mutation might enable formation of an aberrant, super-tight
246 enzyme:substrate ([ES]) complex that does not normally form between the wild type proteins.
247 However, as will be described later on, this hypothesis was rejected based on kinetic arguments.

248 We next sought to determine whether the large differences we observed in K_d values were
249 due to differences in k_{on} or k_{off} . Remarkably, despite a 200-fold difference in K_d for CSN^{5H138A}
250 binding to substrate compared to CSN binding to product, the k_{on} values for formation of these
251 complexes were nearly identical ($2.0 \times 10^7 \text{ M}^{-1} \text{ sec}^{-1}$ for CSN–product and $2.2 \times 10^7 \text{ M}^{-1} \text{ sec}^{-1}$ for
252 CSN^{5H138A}–substrate; Figure 3C). This suggested that the difference in affinity was driven by a
253 large difference in k_{off} . To test this hypothesis, we directly measured k_{off} values for select [ES] and
254 enzyme-product complexes by pre-forming the complex and then adding excess unlabeled
255 Cul1/Rbx1 chase and monitoring the reduction in dansyl fluorescence over time (Figure 3C and
256 Figure 3–figure supplement 3F-I; for this and a subsequent experiment in Figure 4B, we used
257 CSN^{5E76A/5H138A} in one of the assays instead of CSN^{5H138A}; the double mutant behaved like CSN^{5H138A}
258 in that it bound Cul1^d/Rbx1 with the same affinity as shown in Figure 3–figure supplement 3J).
259 Consistent with the predictions from the K_d and k_{on} values, substrate dissociated very slowly from
260 CSN^{5E76A,5H138A}, whereas product dissociated ~65-fold faster from CSN. This suggests that as
261 substrate is deneddylated to product, its affinity for CSN is strongly reduced and its k_{off} speeds up.

262 **The N-terminal domains of Csn2 and Csn4 and the RING of Rbx1 promote enzyme–substrate** 263 **interaction.**

264 Armed with assays to measure binding and deneddylation of substrate, we next sought to
265 test the implications that emerged from our structural analysis of the CSN^{5H138A}–N8-SCF^{Skp2/Cks1}
266 complex. First, we investigated the roles of the NTDs of Csn2 and Csn4, both of which, upon
267 binding substrate, underwent conformational changes and made contact with Cul1 and the RING
268 domain of Rbx1 (Figures 1B–C, Figure 1–figure supplements 1I–K)(Lingaraju et al., 2014). To
269 measure the effect of these mutations on binding to Cul1^d-N8/Rbx1, we combined them with
270 Csn5-H138A to prevent deneddylation. Deletion of the first 269 amino acids of Csn2, observed to
271 interact with Cul1 but not the RING domain of Rbx1, caused a massive loss in binding to substrate
272 ($K_d > 1300 \text{ nM}$; Figure 3B, Figure 3–figure supplement 3K). Thus, the contact we observed
273 between Csn2-NTD and N8-SCF^{Skp2/Cks1} was critical to formation of the [ES] complex. By contrast,
274 deletion of the first 297 amino acids NTD of Csn4 (4ΔN), a portion which was observed to form

275 interfaces with both Cul1 and the RING domain of Rbx1, had a relatively modest effect;
276 CSN^{4ΔN,5H138A} bound Cul1^d/Rbx1 and Cul1^d-N8/Rbx1 with K_d values of > 750 nM and 20 nM,
277 respectively (Figure 3B, Figure 3–figure supplement 3L-M).

278 In addition to the motions of the Csn2 and Csn4 NTDs, our structural analysis revealed
279 formation of substantial interfaces between CSN and the RING domain of Rbx1. To test the role of
280 the RING domain in complex formation, we generated both Cul1/Rbx1 and Cul1^d/Rbx1 in which
281 the RING domain can be deleted by introducing a TEV protease cleavage site (Dougherty et al.,
282 1989) after residue 37 of Rbx1 to generate Cul1 (or Cul1^d)/Rbx1^{TEV} (Figure 4A). This was
283 essential, because it would not be possible to conjugate Nedd8 to Cul1/Rbx1 expressed as a
284 mutant lacking the RING domain. After conjugating Nedd8 to the purified complex, we treated it
285 with TEV protease to remove the RING domain, yielding Cul1 (or Cul1^d)-N8/Rbx1^{ΔRING} (Figure 4A).
286 The truncated Cul1/Rbx1^{ΔRING} was inactive in an ubiquitylation assay (Figure 4–figure supplement
287 4A) but behaved as a monodisperse sample with the expected hydrodynamic radius upon size
288 exclusion chromatography (Figure 4–figure supplement 4B). Notably, Cul1^d-N8/Rbx1^{ΔRING} bound
289 CSN^{5E76A,5H138A} and CSN^{5E76A} with affinities (12 nM and 13 nM respectively; Figure 3B, Figure 3–
290 figure supplement 3N) similar to that observed for binding of wild type Cul1^d-N8/Rbx1 to
291 CSN^{4ΔN,5H138A}. Given the similar effects of the Csn4-ΔNTD and Rbx1-ΔRING mutations on complex
292 formation, we next tested whether their effects arose from loss of the interface that forms
293 between these domains (Figure 1–figure supplement 1K). However, double mutant analysis
294 suggested that the Csn4-ΔN and Rbx1-ΔRING mutations had largely independent effects on
295 binding (Figure 4B). The overall picture that emerged from these studies in light of the structural
296 data is that the interaction of Csn2-NTD with neddylated substrate makes a large contribution to
297 binding energy, with modest enhancements independently provided by the Csn4-NTD and Rbx1-
298 RING domains.

299 **The ‘E-vict’ enables efficient clearance of product from the CSN active site**

300 The striking difference in the K_d for CSN^{5H138A} binding to substrate compared to CSN
301 binding to product suggested that a conformational rearrangement of the [ES] complex occurs
302 upon cleavage of the isopeptide bond, resulting in a large increase in the product k_{off} , thereby
303 preventing the enzyme from becoming product-inhibited. However, we were puzzled by the
304 relatively minor impact of Nedd8 on the affinity of Cul1^d/Rbx1 for CSN^{5H138A}; whereas substrate
305 bound with K_d of 1.6 nM, product binding was only ~6-fold weaker (Figure 3B). Why, then, did

306 CSN bind so much less tightly to product? We reasoned that a key difference between CSN^{5H138A}
307 and CSN is the absence of the active site zinc from CSN^{5H138A}, which prevents formation of a stable
308 apo-CSN complex in which E104 of the INS1 domain of Csn5 is bound to the active site zinc. If this
309 conjecture is correct, it makes the prediction that CSN^{5E104A}, which should also be unable to form
310 stable apo-CSN, should likewise exhibit high affinity for product. This was confirmed: CSN^{5E104}
311 bound Cul1^d/Rbx1 with a K_d of 26 nM (Figure 3B, Figure 3-figure supplement 3O). Furthermore,
312 measurement of k_{off} values revealed that product dissociated from CSN^{5H138A} and CSN^{5E104A} about
313 8-fold more slowly than it dissociated from CSN (Figure 3C). Based on these observations, we
314 propose the ‘E-vict’ hypothesis, which is described in more detail in the Discussion. The essence of
315 this hypothesis is that, following cleavage of the isopeptide bond and dissociation of Nedd8, INS1
316 of Csn5 engages the active site zinc. This accelerates the rate of dissociation of deneddylated
317 Cul1/Rbx1, thereby preventing CSN from becoming clogged with product. We note that Csn5-E76
318 also contributes to the operation of this mechanism, because CSN^{5E76A} bound tightly to product
319 (Figure 3-figure supplement 3P). We speculate that engagement of the active site zinc by Csn5-
320 E104 forces Csn5-E76 into a configuration that promotes egress of product. Further insights into
321 the exact sequence of events that accelerates product dissociation await high-resolution
322 structures of CSN bound to Cul1/Rbx1 in various states.

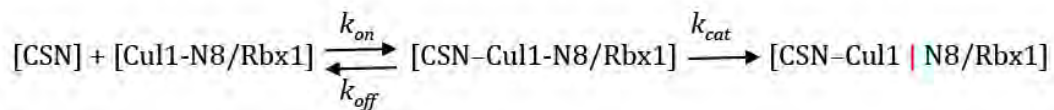
323 **Kinetic effects of binding-defective mutations on substrate deneddylation**

324 We next sought to address the effects of the enzyme and substrate mutations described in
325 the preceding sections on the deneddylation reaction. We previously showed that CSN^{2ΔN} has
326 severely reduced catalytic activity (Enchev et al., 2012), which is consistent with the binding data
327 reported here. CSN^{4ΔN} exhibited a 20-fold defect in substrate cleavage (Figure 5A, Figure 5-figure
328 supplement 5A). Meanwhile, the k_{cat} for cleavage of Cul1-N8/Rbx1^{ΔRING} by CSN was reduced by a
329 staggering ~18,000-fold relative to wild type substrate (Figures 5A–B). Given that the neddylated
330 ΔRING substrate bound to CSN with only modestly reduced affinity, we surmised that the principal
331 defect of this mutant might be its failure either to induce the activating conformational change in
332 CSN, and/or to position accurately the isopeptide bond in the active site. Although we do not have
333 the tools to address the latter point, we queried the former by examining the Csn6-ΔINS2
334 mutation, which partially mimics the effect of substrate binding in that it destabilizes the
335 autoinhibited state (Lingaraju et al., 2014). The Csn6-ΔINS2 mutation slightly weakened binding
336 to wild type product (Figure 3B, Figure 3-figure supplement 3Q) but completely suppressed the

337 modest binding defect of the neddylated Δ RING substrate (Figure 3B, Figure 3-figure supplement
338 3R) and promoted an \sim 8-fold increase in its deneddylation rate (Figure 5-figure supplement 5B).
339 This partial suppression effected by Csn6- Δ INS2 suggests that the RING domain contributes to the
340 constellation of conformational changes in CSN that occur upon substrate binding. Note that the
341 CSN^{6 Δ INS2} enzyme nevertheless exhibited a $> 1,000$ -fold defect towards the Cul1-N8/Rbx1 ^{Δ RING}
342 substrate, strongly indicating further functions of the RING domain, which may include a potential
343 role in substrate positioning as well.

344 A noteworthy feature of the deneddylation reactions carried out with CSN^{4 Δ N} enzyme or
345 Δ RING substrate is that although k_{cat} was reduced in both cases, K_M was also reduced (Figure 5A).
346 Whereas these results imply that deletion of the Csn4-NTD or Rbx1-RING improved affinity of the
347 [ES] complex, our direct binding measurements indicated this was not the case. To understand

Equation 1: Cul1-N8/Rbx1 deneddylation by CSN. The vertical red bar indicates the cleaved bond.



348 this apparent paradox, it is essential to consider the kinetic behavior of CSN-mediated
349 deneddylation. The formal definition of K_M for a deneddylation reaction (Equation 1), as stipulated
350 by Briggs and Haldane (Briggs and Haldane, 1925), is: $K_M = (k_{off} + k_{cat})/k_{on}$. In the special case of
351 Michaelis-Menten kinetics, which is based on the assumption that k_{off} is much larger than k_{cat} the
352 expression simplifies to k_{off}/k_{on} , or K_d . However, k_{cat} for CSN ($\sim 1.1 \text{ sec}^{-1}$) is actually much faster
353 than k_{off} measured for dissociation of substrate from the CSN^{5E76A, 5H138A} mutant (0.017 sec^{-1}). The
354 implication of this is that almost every binding event between CSN and substrate results in
355 catalysis, and K_M (200 nM; Figure 5A and (Emberley et al., 2012) is much larger than K_d (1.6 nM,
356 Figure 3B). But, if k_{cat} is reduced by mutation, the Briggs-Haldane equation predicts that K_M should
357 approach K_d . Indeed, this is exactly what we see for reactions that exhibit reduced k_{cat} , including
358 reactions with mutant CSN^{4 Δ N} enzyme or mutant Δ RING substrate (Figure 5A). In the slowest
359 reaction (cleavage of Cul1/Rbx1 ^{Δ RING} by CSN) the K_M (5 nM) is in the same range as the K_d with
360 which this substrate bound to CSN^{5E76A, H138A} (12 nM; Figure 3B), and approaches the K_d measured
361 for binding of substrate to CSN^{5H138A} (1.6 nM). This provides strong support for our proposal that
362 the CSN^{5H138A}-Cul1^d/Rbx1 complex is representative of the affinity that develops during normal
363 catalysis.

364 **Functional significance of Csn5 INS1 *in vitro* and in cells**

365 To understand the significance of the E-vict mechanism to CSN function *in vitro* and in cells,
366 we measured the k_{cat} for CSN^{5E104A} and observed that it is 2.5-fold slower than for CSN (Figure 5A,
367 Figure 5–figure supplements 5C–E). This was unexpected, because it was reported that the Csn5-
368 E104A mutation enhances the catalytic activity of CSN towards an unnatural substrate (Lingaraju
369 et al., 2014). Interestingly, a similar reduced rate was observed in both single- and multi-turnover
370 reactions, indicating that under our specific reaction conditions, the activating conformational
371 changes/chemical step are affected at least as much as product dissociation. This may not be the
372 case in cells, where substrate receptors and other factors may further stabilize product binding.

373 To test if Csn5-E104 contributes to CSN function *in vivo*, we generated a partial knockout of
374 Csn5 in HEK293T cells using CRISPR/Cas9 (Shalem et al., 2014a). This cell line expressed severely
375 reduced levels of Csn5 and consequently displayed hyper-accumulation of Nedd8-conjugated
376 endogenous Cul1 (Figure 6A), but retained sufficient protein to survive. We introduced either an
377 empty retrovirus or retroviruses coding for Flag-tagged wild type or mutant Csn5 proteins into
378 these cells, and then monitored the Cul1 neddylation status by immunoblotting. In contrast to wild
379 type ^{Flag}Csn5, cells expressing ^{Flag}Csn5-E104A, H138A or E76A did not regain a normal pattern of
380 Cul1 neddylation (Figure 6A). The same was observed for Cul2, Cul3, Cul4A, and Cul5 (Figure 6–
381 figure supplement 6A). Consistent with reduced CSN activity, as revealed by increased cullin
382 neddylation, Skp2 levels were reduced in cells expressing mutant Csn5 proteins (Figure 6A)(Cope
383 and Deshaies, 2006; Wee et al., 2005). To test whether mutations in the catalytic site of Csn5
384 resulted in increased affinity for Cul1, we immunoprecipitated wild type and mutant ^{Flag}Csn5
385 proteins and probed for co-precipitation of endogenous Cul1. In addition to the mutants described
386 above, we surveyed a much broader panel of catalytic site substitutions to determine whether the
387 results observed in our *in vitro* experiments were specific to the mutations employed or were a
388 general consequence of disrupting the active site. As shown in Figure 6B, the results were
389 concordant with what was observed *in vitro*. On the one hand, ^{Flag}Csn5–H138A retrieved high
390 levels of Cul1-N8. The same was true for ^{Flag}Csn5 carrying mutations in other core residues of the
391 JAMM domain (e.g. H140 and D151)(Cope et al., 2002). On the other hand, ^{Flag}Csn5-E104A
392 retrieved high levels of unmodified Cul1. We propose that this arises from its ability to bind and
393 deneddylate substrate (albeit at a reduced rate), but then remain tightly bound to the product due
394 to loss of the E-vict mechanism.

395 The unexpected reduction in activity observed for Csn5-E104A both *in vitro* and in cells
396 (Figures 5A, 6A) suggested that the adjacent residue, T103, may also be important for
397 deneddylation. A T103I mutation in *Drosophila melanogaster* impedes proper interaction of
398 photoreceptor neurons with lamina glial cells in the developing brain. If this mutant also causes a
399 loss of CSN deneddylase activity, it would explain the recessive nature of this mutation in flies
400 (Suh et al., 2002). Indeed, like Csn5-E104A, Csn5-T103I did not restore a normal Cul1 neddylation
401 pattern when expressed in Csn5-depleted cells (Figure 6C) and exhibited low deneddylase activity
402 *in vitro* (Figures 5A, Figure 5-figure supplement 5F). In contrast to CSN^{5E104A}, however, CSN^{5T103I}
403 bound Cul1^d/Rbx1 product with low affinity, both *in vitro* (Figure 3B, Figure 3-figure supplement
404 3S) and in cells (Figure 6B). Therefore, although CSN^{5E104A} and CSN^{5T103I} both have diminished
405 catalytic activity, their defects appear to have distinct molecular bases. To further explore the
406 divergent effects of Csn5-E104A and Csn5-T103I mutations on Cul1 binding, HEK293T stably
407 expressing wild type or mutant versions of FlagCsn5 were grown in ‘heavy’ SILAC medium (wild
408 type), or ‘light’ SILAC medium (mutants). Each mutant lysate was individually mixed with wild
409 type lysate, and then subjected to immunoprecipitation and SILAC mass spectrometry. Whereas
410 all CSN subunits exhibited light:heavy ratios of ~1 (Figure 6-figure supplement 6B), the FlagCsn5-
411 E104A pull-down showed elevated levels of all cullins compared to wild type, whereas FlagCsn5-
412 T103I pulled down cullins at levels equal to or less than wild type FlagCsn5 (Figure 6D).

413 Discussion

414 ‘Induced fit’ underlies interaction of substrate with CSN and triggers enzyme activation

415 Figure 7 displays a model that incorporates published data and data presented in this
416 manuscript. Panels A-C shows a schematic view of the structural transitions that occur upon
417 substrate binding, and collectively contribute to efficient catalysis, whereas panel D provides the
418 rate constants for the deneddylation cycle. We tentatively propose the following sequence of
419 events. Free CSN exists in an inactive state in which E104 of Csn5-INS1 forms a fourth ligand to
420 zinc (Figure 7A)(Lingaraju et al., 2014). In this state the NTDs of both Csn2 and Csn4 are in “open”
421 conformations relative to the cullin substrate, and the MPN domains of Csn5/Csn6 are in a distal
422 position relative to it. Substrate binds this state rapidly (Figure 7B), likely driven by electrostatic
423 interactions between Cul1 and Csn2-NTD. This would account for the similar, extremely fast k_{on}
424 values that we measured for different combinations of Cul1^d/Rbx1 and CSN. Binding of CSN to
425 neddylated substrate results in a series of conformational changes in both complexes (Figure 7B).

426 These include (i) the translocation of the N-terminal helical repeats of Csn2 towards the CTD of
427 Cul1, (ii) the movement of the NTD of Csn4 towards the RING domain of Rbx1 and the WHA
428 domain of Cul1, (iii) the translocation of the MPN domains of Csn5–Csn6 towards the neddylylated
429 WHB domain of Cul1, (iv) movement of the WHB domain towards Csn5, (v) the opening of the
430 interface between Nedd8 and the WHB domain, and (vi) the formation of a new interface between
431 Csn5 and Nedd8 probably involving the hydrophobic patch of Nedd8 and neighboring residues, as
432 well as a tenuous interface between the WHB and the Rbx1 RING domain. Furthermore, although
433 not structurally resolved in the present study, movements of Csn5-E76 and E104 towards and
434 away from the zinc atom (vii), respectively, probably similar to the conformation reported in
435 (Echalier et al., 2013), must occur to enable catalysis. Finally, a series of other unresolved
436 movements are likely to be germane including (viii) positioning of the extended C-terminus of
437 Nedd8, and the corresponding portion of the WHB domain for catalysis as well as contacts
438 between the INS1 and INS2 domains of Csn5 and the WHB domain of Cul1.

439 To probe the significance of the conformational changes summarized above, we generated
440 and analyzed mutant enzymes. Deletion of Csn2-NTD virtually eliminated substrate binding
441 (Figure 3–figure supplement 3K), suggesting that movement of this domain (motion i) enables a
442 high affinity interaction between CSN and neddylylated CRLs. Meanwhile a mutant lacking Csn4-
443 NTD, CSN^{4ΔN,5H138A}, bound Cul1-N8/Rbx1 ~10-fold less tightly than CSN^{5H138A}, albeit still with a
444 relatively high affinity (20 nM, Figure 3B). A similar effect on binding affinity was seen with a
445 substrate lacking the RING domain of Rbx1 (Figure 3B). Even though the RING and Csn4-NTD
446 domains are adjacent in the enzyme-substrate [ES] complex (Figure 1), double mutant analysis
447 suggests that they make substantially independent contributions to binding energy (Figure 4B).
448 Interestingly, enzyme assays revealed a much greater effect of deleting the RING than deleting the
449 Csn4-NTD, suggesting that the RING domain makes a profound contribution to catalysis in a
450 manner that does not depend on its proximity to Csn4-NTD. We do not know the extent to which
451 the reduced catalytic rates for these mutants arise from defects in enzyme activation versus
452 substrate positioning, but we note that cleavage of ΔRING substrate was accelerated by ~8-fold
453 upon deletion of Csn6-INS2, suggesting that at least a small part of the problem with this substrate
454 is that it failed to properly trigger activating conformational changes in CSN.

455 In addition to the movements of individual domains, formation of the [ES] complex is
456 accompanied by wholesale translocation of the Csn5 and Csn6 subunits. We suggest that this

457 motion contributes primarily a k_{cat} effect, because deletion of Csn6-INS2, which is proposed to
458 facilitate this motion, enhanced k_{cat} but had no noteworthy impact on binding to substrate (Figure
459 3B), and removal of Csn5 from the complex did not substantially affect CSN assembly with
460 substrate (Enchev et al., 2012). We cannot conclude much about the other motions enumerated
461 above, but we note that mutations that are predicted to reside near the interface of the Csn5-INS2
462 and Cul1-WHB domains cause significant reductions in substrate deneddylation (Figure 1–figure
463 supplements 1N–O). In addition, reorientation of Nedd8 away from Cul1-WHB and towards Csn5
464 as predicted here is consistent with the prior observation that the hydrophobic patch of Nedd8
465 recruits UBXD7 to neddylated CRLs (den Besten et al., 2012). Presumably, the conformational
466 changes that occur during the activation process are connected in some manner. Interestingly,
467 CSN^{5E104A} and CSN^{6 Δ INS2} both cleave ubiquitin-rhodamine at 0.04 sec⁻¹ (which is ~6-fold faster than
468 wild type CSN), but CSN^{5E104A,6 Δ INS2} is yet 5-fold faster (0.2 sec⁻¹) than either single mutant
469 (Lingaraju et al., 2014). The activities of the single and double mutants imply that the Csn6- Δ INS2
470 mutation must destabilize binding of Csn5-E104 to the catalytic zinc, but only in a small fraction
471 ($\leq 20\%$) of complexes. Meanwhile, movements at the Csn4/6 interface must do more to the active
472 site than simply disrupt the interaction of Csn5-E104 with the catalytic zinc, implying the
473 existence of at least two inputs to CSN activation. Resolving how binding of substrate is connected
474 to enzyme activation awaits high-resolution structural analyses of the enzyme and substrate in
475 various states.

476 **A kinetic model for the CSN enzyme cycle reveals an essential role for the E-vict mechanism** 477 **in sustaining rapid catalysis**

478 Upon formation of an [ES] complex, the conformational changes that occur in both CSN and
479 substrate culminate in cleavage of the isopeptide bond that links Nedd8 to cullin. Although we
480 don't know the microscopic rate constants for the various conformational changes and bond
481 cleavage, all evidence points to the former being slower than the latter, which can occur with $k \geq$
482 6.3 sec⁻¹, based on the k_{cat} for cleavage of N8-CRL4A^{DDB2} by CSN^{6 Δ INS2} (Lingaraju et al., 2014). The
483 actual cleavage may be even faster because this measurement was made under multi-turnover
484 conditions, in which case product dissociation may have been rate limiting. Regardless, the sum
485 total rate of the activating conformational motions plus isopeptide bond cleavage reported here
486 (~ 1 sec⁻¹) is considerably faster than substrate dissociation from CSN^{5H138A} (~ 0.017 sec⁻¹),
487 indicating that CSN conforms to Briggs-Haldane kinetics and essentially every [ES] complex that

488 forms proceeds to cleavage, the physiological implications of which are considered in the next
489 section.

490 Cleavage of the isopeptide bond initiates a series of events leading to product release.
491 Removal of Nedd8 increases dissociation of Cul1/Rbx1 by ~7-10 fold. We propose that
492 dissociation of the cleaved Nedd8 also removes an impediment to Csn5-INS1, which can now bind
493 the catalytic site zinc via E104 to return CSN to its apo state. This engagement, which we refer to
494 as the 'E-vict' mechanism, is a critical step in what is likely to be a series of conformational
495 rearrangements that include repositioning of Csn5-E76. Collectively, these movements reduce the
496 affinity of CSN for product and accelerate its rate of dissociation by an additional order of
497 magnitude. The removal of Nedd8 and E-vict together bring about an ~100-fold loss in affinity of
498 Cul1/Rbx1 for CSN. The slow dissociation of product from CSN mutants that were unable to
499 undergo E-vict (0.12-0.16 sec⁻¹; Figure 3C) suggests that this mechanism is important for
500 maintaining physiological rates of CRL deneddylation. This is further supported by the
501 observation that Csn5-E104A, but not wild type Csn5, co-precipitates substantial amounts of
502 deneddylated Cul1 from cells (Fig. 6B). Slow clearance of product could explain, in part, the failure
503 of this mutant to complement a Csn5 deficiency (Fig. 6A). The E-vict mechanism presents an
504 elegant solution to a fundamental challenge facing enzymes: how to achieve high specificity
505 without compromising rapid turnover.

506 We note that the product k_{off} for Cul1^d/Rbx1 (1.1 sec⁻¹) is similar to the k_{cat} we measured
507 for both single- and multi-turnover reactions. This suggests that depending on the exact structure
508 of the neddylated CRL substrate, the rate-limiting step may vary from one deneddylation reaction
509 to another. Regardless, our biochemical and cell-based data suggest that if the E-vict mechanism
510 did not exist, product dissociation would become the Achilles heel of deneddylation reactions.

511 **CSN in its cellular milieu**

512 The kinetic parameters reported here coupled with quantitative measurements of protein
513 concentrations by selected reaction monitoring mass spectrometry ((Bennett et al., 2010) and J.R.
514 and R.J.D., unpublished data) allow a preliminary estimate of the steady-state distribution of CSN
515 in cells. The total cullin concentration in the 293T cell line used in this work is ~2200 nM.
516 Meanwhile, the CSN concentration is ~450 nM. Although the total amount of Nedd8-conjugated
517 cullins was not measured, immunoblot data suggest that ~1000 nM is a reasonable estimate. The

518 K_d reported here for the [ES] complex (~ 2 nM), thus predicts potentially near-complete saturation
519 of the cellular CSN pool with neddylated cullins. This implies that formation of new [ES]
520 complexes is limited by the slowest step in the catalytic cycle, i.e. either the conformational
521 rearrangements or product dissociation. *In vitro*, CSN follows Briggs-Haldane kinetics and cleaves
522 Nedd8 off nearly every neddylated CRL that it binds. Because CSN is not in equilibrium with its
523 substrates in our simplified *in vitro* system, it cannot rely on differences in substrate K_d to achieve
524 specificity. Thus, differences in k_{off} on the order of ≤ 10 -fold, which might occur with different
525 cullins or substrate adaptors, would be predicted to have minimal effects on catalytic efficiency
526 provided that k_{on} remains roughly the same, as was observed for different configurations of
527 substrate and product in this study. Importantly, this parameter can potentially be profoundly
528 altered by ubiquitylation substrates, E2 enzyme, or other *in vivo* binding partners of Nedd8-
529 conjugated CRLs, which compete with CSN (Emberley et al., 2012; Enchev et al., 2012; Fischer et
530 al., 2011) and thus should reduce its apparent k_{on} . It is also conceivable that binding partners
531 might alter the partitioning of the CSN-N8-CRL complex either by increasing k_{off} and/or reducing
532 k_{cat} , such that N8-CRL bound to an ubiquitylation substrate dissociates prior to completion of the
533 conformational rearrangements that culminate in its deneddylation.

534 Based on measurements reported here, it is likely that CSN complexes in cells are
535 constantly undergoing catalysis, dissociating rapidly from product, and rebinding other CRLs on
536 the time-scale of a few seconds or less. Consistent with this picture, addition of a Nedd8
537 conjugation inhibitor to cells leads to nearly complete disappearance of neddylated cullins within
538 5 minutes, and this does not account for the time it takes the drug to equilibrate across the
539 membrane and deplete the cellular pool of Nedd8~Ubc12 thioesters (Soucy et al., 2009). The
540 dynamic properties of CSN measured here reveal a CRL network of extreme plasticity that can be
541 reconfigured in minutes to respond to changing regulatory inputs. Although quantitative studies
542 of CRL network dynamics remain in their infancy, it is evident that the tools are at hand to begin to
543 understand how these remarkable enzymes function and are regulated within cells.

544 **Materials and Methods**

545 *Cloning* All eight wild type CSN subunits were cloned into a single pFBDM baculovirus transfer
546 MultiBac vector (Berger et al., 2004). His₆-Csn5 was inserted into the first multiple cloning site (MCS1)
547 of a pFBDM vector using NheI/XmaI and Csn1 was put into MCS2 of the same vector with BssHII/NotI.
548 Similarly, Csn2 was inserted into a second pFBDM vector using BssHII/NotI and StrepII^{2x}-Csn3,

549 containing an N-terminal PreScission-cleavable StrepII^{2x}-tag, using NheI/XmaI. From this plasmid the
550 Csn2/StrepII^{2x}-Csn3 gene cassette was excised out with AvrII/PmeI and inserted into pFBDM^{Csn1/His6Csn5},
551 whose multiplication module had been linearized with BstZ17I and SpeI, yielding pFBDM^{Csn1/His6-}
552 Csn5/Csn2/StrepII2x-Csn3. A pFBDM^{Csn4/Csn7b} vector was generated using BssHII/NotI to insert Csn4 and
553 NheI/XmaI for Csn7b, and the resultant gene cassette was inserted into linearized pFBDM^{Csn1/His6-}
554 Csn5/Csn2/StrepII2x-Csn3, resulting in pFBDM^{Csn1/His6-Csn5/Csn2/StrepII2x-Csn3/Csn4/Csn7b}. Finally, a pFBDM^{Csn6/Csn8}
555 vector was generated using BssHII/NotI for Csn6 and NheI/XmaI for Csn8 insertion. Once again the
556 resultant gene cassette was inserted into linearized pFBDM^{Csn1/His6-Csn5/Csn2/StrepII2x-Csn3/Csn4/Csn7b}, yielding
557 the full wild type CSN vector pFBDM^{Csn1/His6-Csn5/Csn2/StrepII2x-Csn3/Csn4/Csn7b/Csn6/Csn8}. A similar cloning
558 strategy was applied for the generation of CSN^{5E76A}, CSN^{5E76A, H138A}, CSN^{5E212R, D213R} and CSN^{4ΔN1-297},
559 except that site-directed mutageneses were performed on pFBDM^{Csn1/His6Csn5} and pFBDM^{Csn4/Csn7b}
560 respectively. CSN^{5E104A} and CSN^{5T103I} were generated with the same general approach, except that that
561 site-directed mutagenesis and sequence validation were performed on a pCRIITPOPO plasmid
562 (Invitrogen) containing StrepII^{2x}-Csn5. Those mutants were then ligated into a MCS1 linearized
563 pFBDM^{Csn1} plasmid. For the production of CSN^{6ΔIns2} we used co-expression from two separate viruses.
564 To this end we applied site-directed mutagenesis on the pFBDM^{Csn6/Csn8} vector to delete amino acids
565 174-179 in Csn6, generating pFBDM^{Csn6ΔIns2/Csn8}. The gene cassette of the latter was excised out using
566 AvrII/PmeI and inserted into BstZ17I/SpeI linearized pFBDM^{Csn4/Csn7b}, yielding
567 pFBDM^{Csn4/Csn7b/Csn6ΔIns2/Csn8}. The resultant bacmid was used together with a bacmid generated from
568 pFBDM^{Csn1/His6-Csn5/Csn2/StrepII2x-Csn3} in order to generate two baculoviruses, which were used for co-
569 infection to generate CSN^{6ΔIns2}. An analogous strategy was applied to generate CSN^{4ΔN/6ΔIns2},
570 CSN^{5H138A/6ΔIns2} and CSN^{5H138A/4ΔN}.

571 The TEV site in Rbx1 as well as mutations in the WHB domain of Cul1 were obtained by site-directed
572 mutagenesis on the pFBDM-Cul1/Rbx1 vector described in (Enchev et al., 2010), which further
573 contained a C-terminal sortase tag described in the next section. Cloning of Cul3/Rbx1 used in the
574 crosslinking/mass spectrometry experiments, Nedd8-pro-peptide-StrepII^{2x} and StrepII^{2x}-Den1 are
575 described in (Orthwein, 2015). Recombinant bacmid and virus generation as well as protein expression
576 proceeded as described in (Enchev et al., 2012). All genes were validated by sequencing as wild type or
577 mutant.

578 *Protein Purification and modifications* CSN and its mutant forms were purified as described in Enchev
579 et al. (2012). Nedd8-activating and conjugating enzymes were purified as described in Emberley et al.
580 (2012) and Enchev et al. (2012). Fluorescently-labeled Cul1 substrates were conjugated with untagged

581 Nedd8. Cull1-sortase was designed with GGGGSLPETGGHHHHHH inserted after the final amino acid
582 of Cull1 into the pGEX vector described in Emberley et al. (2012). All sortase reactions were done at
583 30 °C overnight with 30 μM Cull1/Rbx1, 50 μM Sortase and 250 μM GGGGK-dansyl in 50 mM Tris pH
584 7.6, 150 mM NaCl and 10 mM CaCl₂ and purified by size exclusion chromatography to yield
585 Cull1^d/Rbx1. Cull1^d/Rbx1 was neddylated and purified as in Emberley et al. (2012) to yield Cull1^d-
586 N8/Rbx1. Cand1 and Sortase were purified as described in Pierce et al. (2013). Production of Cull1/Rbx1
587 and Cul3/Rbx1 baculovirus constructs used for electron microscopy and crosslinking mass spectrometry,
588 bacterial split-and-co-express Cull1/Rbx1^{ΔRING}, Nedd8 with native N- and C-termini, used for electron
589 microscopy and crosslinking mass spectrometry and for the experiments involving Cull1/Rbx1^{TEV}, Den1
590 as well as the respective preparative neddylation were performed as described in Enchev et al. (2012)
591 and (Orthwein et al., 2015). Den1 was used in 1:50 ratio for 10 min at 25 °C to remove poly-neddylation.
592 Cull1/Rbx1 complexes with mutations in the WHB domain of Cull1 (Figure 1–figure supplement 1N, O)
593 and Cull1/Rbx1^{TEVΔRING} were purified from High Five insect cells as described in Enchev et al. (2010).
594 Dansylation of Cull1/Rbx1 variants expressed in insect cells was performed for 8 to 12 h at 30 °C while
595 spinning at 5000 g, and purified by passing the dansylation reaction through a 5 ml HisTrap FF column
596 (GE Healthcare) in 50 mM Tris-HCl, pH 7.6, 400 mM NaCl, 20 mM imidazole. The Cull1^d/Rbx1-
597 containing flow through was concentrated, neddylated (if required), and further purified over a Superdex
598 200 size exclusion column (GE Healthcare) equilibrated with 15 mM HEPES, pH 7.6, 150 mM NaCl, 2
599 mM DTT, 2 % (v/v) glycerol. Neddylation of Cull1/Rbx1^{TEVΔRING} was performed at 25 °C for 12-14 h in
600 50 mM Tris-HCl, pH 7.6, 100 mM NaCl, 2.5 mM MgCl₂, 150 μM ATP, spinning at 2000 g, and was
601 followed by 30 min incubation with 1:50 (w/w) Den1 to remove poly-neddylation. The reaction was
602 purified over a Strep-Tactin Superflow Cartridge (QIAGEN), and eluted in 15 mM HEPES, pH 7.6, 250
603 mM NaCl, 2 mM DTT, 2 % (v/v) glycerol, 2.5 mM *d*-desthiobiotin. RING cleavage was performed for
604 12-14 hours at 25 °C, spinning at 2000 g, in the presence of 100 mM EDTA, pH 8 and 1:1 (w/w) TEV.
605 Dansylation proceeded as described above.

606 *Deneddylation Assays* All deneddylation assays were performed in a buffer containing 25 mM Tris-HCl,
607 pH 7.5, 100 mM NaCl, 25 mM trehalose, 1 mM DTT, 1 % (v/v) glycerol, 0.01 % (v/v) Triton X-100 and
608 0.1 mg/ml ovalbumin or BSA. Radioactive deneddylation reactions with bacterially expressed substrates
609 were done as described (Emberley et al., 2012). Radioactive deneddylation reactions with substrates
610 expressed in insect cells were performed at 24 °C with 0.5 nM CSN (Figure 2–figure supplement 2C) or
611 2 nM CSN (Figure 5B). All remaining radioactive deneddylation reactions were performed with
612 bacterially expressed Cull1-N8/Rbx1 substrates (50 nM) and 2 nM CSN unless otherwise noted. Single-

613 turnover reactions were done with 25 nM Cul1 substrates and 1 μ M CSN on a Kintek RQF-3 Rapid
614 Quench Flow at 24 °C. Single-turnover data were fit to one phase decay function: $Y=(Y_0 - EP)*\exp(-$
615 $k_{cat}*X) + EP$ (where EP corresponds to reaction end point value), to determine the k_{cat} . Deneddylation
616 assays in Figure 1–figure supplement 1N, O were performed with 800 nM substrate and 20 nM enzyme
617 and visualized by Coomassie stain. Depending on the exact protein preparations used and the laboratory,
618 we observed rates for the wild type reaction ranging from 1.1-2.6 sec^{-1} .

619 *Fluorescence Assays* All assays were performed in a buffer containing 30 mM Tris pH 7.6, 100 mM
620 NaCl, 0.25 mg/ml ovalbumin or BSA and 0.5 mM DTT with 30 nM dansyl-labeled Cul1/Rbx1 and
621 titrated concentrations of CSN. The mixtures were allowed to reach equilibrium by incubation at room
622 temperature for ~ 10 minutes prior to measurements. Equilibrium binding assays using Cul1/Rbx1
623 variants expressed in insect cells (Figure 2, Figure 2–figure supplement 2E, Figure 3–figure supplement
624 3N, 3R, Figure 4B) were read at 530 nm on a CLARIOstar plate reader (BMG Labtech) in 384-well
625 plates (Corning, low flange, black, flat bottom), 90 μ l per well, while binding assays using bacterially
626 expressed Cul1/Rbx1 variants were performed on a Fluorolog-3 (Jobin Yvon) (all other binding data
627 figures). Binding assay with Cul1^d-N8/Rbx1 (substrate) and CSN^{5E76A} were allowed to equilibrate for
628 only 45 seconds, because although this mutant exhibited an ~ 300 -fold decrease in activity (data not
629 shown) the residual activity was high enough to cause substantial deneddylation in a 10 minute
630 incubation. It should be noted that several of the K_d values reported for CSN binding to Cul1^d-N8/Rbx1
631 or Cul1^d/Rbx1 are below the concentration of the dansylated ligand (30 nM). While this is generally not
632 the preferred approach, we found that 30 nM was the lowest concentration that consistently yielded
633 highly reproducible results. The estimated K_d is very sensitive to the density of data points at the
634 inflection point of the curve, and thus these estimates can be more prone to error. Nevertheless, different
635 investigators in Zurich and Pasadena have consistently obtained an estimate of 1.6-5 nM for binding of
636 CSN^{5H138A} to Cul1^d-N8/Rbx1 and of 9-13 nM for binding to CSN^{5H138A} to Cul1^d/Rbx1, using different
637 protein preparations. To estimate K_d , all data points were fitted to a quadratic equation, $Y = Y_0 + (Y_{\text{max}} -$
638 $Y_0) * (K_d + A + X - \sqrt{(K_d + A + X)^2 - 4A * X}) / 2 * A$ where A equals concentration of labeled protein, using
639 Prism (Graph Pad). On-rate and off-rate measurements were performed on a Kintek Stopped-flow SF-
640 2004 by exciting at 340 nm and collecting emissions through a 520 \pm 20 nm filter. For off-rate
641 measurements, the concentrations of proteins used in each reaction are provided in the legend of Figure
642 3–figure supplements 3F–I. Off rate data were fit to one phase decay function: $Y=(Y_0 - EP)*\exp(-$
643 $k_{off}*X) + EP$ (where EP corresponds to reaction end point value). Whereas K_d , on-rate, and off-rate
644 measurements with different configurations of Cul1 or different CSN mutants are directly comparable,

645 off-rate measurements are not directly comparable to k_{cat} measurements and may differ from expectation
646 by a few fold because different buffers were used, the Cull1/Rbx1 preparations were from different
647 sources (bacterial for k_{cat} , baculoviral for k_{off}), and the Cull1/Rbx1 preparations carried different labels
648 (dansylated Cull1 for k_{off} , [32 P]-Nedd8 for k_{cat}).

649 *Cell Culture and SILAC Mass Spectrometry* Cells were grown in Lonza DMEM containing 10% FBS
650 (Invitrogen). Transient transfections were done with FugeneHD per the manufacturers instructions
651 (Roche). Flag-tagged *CSN5* coding sequences were cloned into a modified MSCV-IRES-GFP vector
652 (containing a pBabe multiple cloning site) via BamHI and EcoRI. Lenti-CRISPR constructs were made
653 as described (Shalem et al., 2014b) using the targeting sequences 5'-
654 CACCGCTCGGCGATGGCGGCGTCC - 3' and 3' - AAACGGACGCCCATCGCCGAGC - 5'.
655 Lenti- and retroviruses were produced in 293T cells and the supernatant subsequently used for
656 transduction to establish stable cell lines. For Western Blot analysis cells were directly lysed in 2X SDS
657 sample buffer. Lysates were sonicated for 15 seconds at 10 % of maximum amplitude using a Branson
658 Digital Sonifier and boiled for 10 minutes at 100 °C. SILAC labeling was in Invitrogen DMEM
659 containing 10% FBS and $^{13}\text{C}_6^{15}\text{N}_2$ -lysine and $^{13}\text{C}_6$ -arginine from Cambridge Isotope Laboratory. For
660 immunoprecipitations, cells were lysed in Pierce Lysis Buffer containing cOmplete Protease Inhibitor
661 Cocktail (Roche) and lysates were sonicated for 10 seconds at 10 % of maximum amplitude using a
662 Branson Digital Sonifier. After a 5 minute clearing at 18000 x g at 4°C, proteins were
663 immunoprecipitated with M2 Flag agarose beads (Sigma) for 30 minutes and prepared for mass
664 spectrometry as described in Pierce et al. (2013). Samples were analyzed using an EASY-nLC 1000
665 coupled to an Orbitrap Fusion and analyzed by MaxQuant (v 1.5.0.30).

666 Digested peptides (250 ng) were loaded onto a 26-cm analytical HPLC column (75 μm ID)
667 packed in-house with ReproSil-Pur C_{18}AQ 1.9 μm resin (120 Å pore size, Dr. Maisch, Ammerbuch,
668 Germany). After loading, the peptides were separated with a 120 min gradient at a flow rate of 350
669 nL/min at 50°C (column heater) using the following gradient: 2-6% solvent B (7.5 min), 6–25% B (82.5
670 min), 25-40% B (30min), 40-100% B (1min), and 100% B (9 min) where solvent A was 97.8% H_2O , 2%
671 ACN, and 0.2% formic acid) and solvent B was 19.8% H_2O , 80% ACN, and 0.2% formic acid. The
672 Orbitrap Fusion was operated in data-dependent acquisition (DDA) mode to automatically switch
673 between a full scan ($m/z=350-1500$) in the Orbitrap at 120,000 resolving power and a tandem mass
674 spectrometry scan of Higher energy Collisional Dissociation (HCD) fragmentation detected in ion trap
675 (using TopSpeed). AGC target of the Orbitrap and ion trap was 400,000 and 10,000 respectively.

676 *SILAC MS data analysis.* Thermo RAW files were searched with MaxQuant (v 1.5.3.8) (Cox and Mann,
677 2008; Cox et al., 2011). Spectra were searched against human UniProt entries (91 647 sequences) and a
678 contaminant database (245 sequences). In addition, spectra were searched against a decoy database
679 (generated by reversing the target sequences) to estimate false discovery rates. Trypsin was specified as
680 the digestion enzyme with up to two missed cleavages allowed. Variable modifications included
681 oxidation of methionine and protein N-terminal acetylation. Carboxyamidomethylation of cysteine was
682 specified as a fixed modification. SILAC was specified as the quantitation method with Arg6 and Lys8
683 specified as the heavy labeled amino acids. Precursor mass tolerance was less than 4.5 ppm after
684 recalibration and fragment mass tolerance was 0.5 Da. False discovery rates at the peptide and protein
685 levels were less than 1% as estimated by the decoy database search. Ratios were calculated for proteins
686 quantified in at least two of the four biological replicates. 95% confidence intervals and adjusted p-
687 values were calculated using the R package limma (Ritchie et al., 2015)

688
689 *Cross-linking coupled to mass spectrometry (XL-MS)* Chemical cross-linking of purified complexes was
690 performed using DSS H₁₂/D₁₂ (Creative Molecules) as cross-linking agent and as previously described
691 (Birol et al., 2014). Subsequent MS analysis and cross-link assignment and detection were carried
692 out essentially as described (Leitner et al., 2014) on an Orbitrap Elite (Thermo Scientific) using the
693 *xQuest/xProphet* software pipeline.

694 *Western Blot Analysis* Proteins were separated by SDS-PAGE gel electrophoresis and transferred to a
695 nitrocellulose membrane by wet blot. Primary antibodies used for detection were: anti-CSN5 mouse
696 monoclonal Santa Cruz Biotechnology sc-393725, anti-Cul1 mouse monoclonal Santa Cruz
697 Biotechnology sc-17775, anti-Cul2 rabbit polyclonal Thermo Scientific #51-1800, anti-Cul3 rabbit
698 polyclonal Cell Signaling #2769, anti-Cul4A rabbit polyclonal Cell Signaling #2699, anti-Cul5 rabbit
699 polyclonal Bethyl Laboratories A302-173A, anti-β-actin mouse monoclonal Sigma A5316, anti-GFP
700 mouse monoclonal Clontech #632381.

701 *Sample preparation for electron microscopy and data collection.* CSN^{5H138A}-SCF-Nedd8^{SKp2/Cks1} samples
702 for cryo-electron microscopy were generated by pre-incubating the purified components as described in
703 Enchev et al (2012) and ran over a Superose 6 increase 3.2/300 column (GE Healthcare) at 4 °C, eluting
704 50 µl fractions in 15 mM HEPES, pH 7.6, 100 mM NaCl, 0.5 mM DTT. The sample was kept on ice and
705 its homogeneity and mono-dispersity from the peak elution was immediately confirmed by visualization
706 in negative stain. For cryo EM preparation, the sample was diluted to 0.1 mg/ml and 2 µl were applied
707 to Quantifoil grids (R1.2/1.3 Cu 400 mesh), freshly coated with an extra layer of thin carbon and glow-

708 discharged for 2 min at 50 mA and 0.2 mbar vacuum. The grids were manually blotted to produce a thin
709 sample film and plunge-frozen into liquid ethane. Data were collected automatically using EPU software
710 in low dose mode on a Titan Krios transmission electron microscope, equipped with a Falcon II direct
711 electron detector (FEI), and operated at 300 kV, an applied nominal defocus from -2.5 to - 5.0 μm in
712 steps of 0.25 μm , and 80,460-fold magnification, resulting in a pixel size of 1.74 \AA on the sample scale.
713 Images were collected as seven separate frames with a total dose of 25 $\text{e}^-/\text{\AA}^2$.

714 *Electron microscopy data analysis.* CTF-estimation and subsequent correction were performed using
715 RELION (Scheres, 2012) and CTFFIND3 (Mindell and Grigorieff, 2003). All micrographs were initially
716 visually inspected and only those with appropriate ice thickness as well as Thon rings in their power
717 spectra showing regularity and extending to 6 \AA or beyond were used for subsequent analysis. In order
718 to generate 2D references for automated particle selection, $\sim 4,000$ single particles were manually
719 picked and subjected to 2D classification in RELION. Six well-defined 2D class averages were selected,
720 low-pass filtered to 35 \AA to prevent reference bias, and used as references. Approximately 150,000
721 single particles were automatically selected and subjected to reference-free 2D and 3D classification, in
722 order to de-select the particles, which resulted in poorly defined or noisy averages. Approximately half
723 of these single particles resulted in a well-defined 3D class average, which resembled the previously
724 published negative stain EM map of the same complex (Enchev et al., 2012). This dataset was subject to
725 3D auto-refinement in RELION, using a version low-pass filtered to 50 \AA as an initial reference. The
726 converged map was further post-processed in RELION, using MTF-correction, FSC-weighting and a
727 soft spherical mask with a 5-pixel fall-off.

728 *Modeling, docking and visualization.* Csn7b was modeled using Csn7a as a template on the Phyre2
729 server (Kelley et al., 2015) and the modeled coordinates were aligned to Csn7a in PDB ID 4D10
730 (Lingaraju et al., 2014), effectively generating a CSN atomic model for the Csn7b-containing complex.
731 Model visualization, molecular docking, distance measurements and morph movie generation were
732 performed with UCSF Chimera (Pettersen et al., 2004).

733 *Accession code.* The cryo electron microscopy density map of CSN^{Csn5H138A}-SCF-Nedd8^{Skp2/Cks1} is
734 deposited in the Electron Microscopy Data Bank under accession code EMD-3401.

735 **Acknowledgements**

736 We thank B. Schulman for Skp1/Skp2 protein as well as for expression plasmids and E. Morris for
737 thin carbon for EM grids. We thank A. Bernini and A. Ragheb for technical assistance with protein

738 work, P. Tittmann for technical support at the ScopeM facility, members of the Ban lab for advice
739 and Annie Moradian and Roxana Eggleston-Rangel for mass spectrometry support at PEL. We also
740 are grateful to S.O. Shan, E. Morris and T. Stuwe for advice and A. Smith, S.O. Shan, and D. Barford
741 for comments on the manuscript. R.M. was supported by a Lee-Ramo Life Sciences Fellowship,
742 R.I.E. was supported by an ETH Pioneer, a Marie Curie and an EMBO short-term fellowship, and
743 A.S. by a Marie Curie fellowship. F.S. acknowledges funding from the Wellcome Trust (Grant
744 095951) and the German Science Foundation Collaborative Research Center (SFB) 969. The Peter
745 laboratory is funded by an ERC advanced grant, the SNF and ETHZ, and the Aebersold laboratory
746 is supported by ETH Zurich, SystemsX.ch and an ERC advanced grant. This work was supported in
747 part by NIH CA164803 to R.J.D. R.J.D. is an Investigator of and was supported by the Howard
748 Hughes Medical Institute. M.J.S and S.H were supported by the Gordon and Betty Moore
749 Foundation, through Grant GBMF775 and the Beckman Institute.

750

751

References

752

- 753 Ambroggio, XI, Rees, DC, Deshaies, RJ 2004. JAMM: A Metalloprotease-Like Zinc Site in the
754 Proteasome and Signalosome. *PLoS Biol* 2: E2.
- 755 Bennett, EJ, Rush, J, Gygi, SP, Harper, JW 2010. Dynamics of cullin-RING ubiquitin ligase network
756 revealed by systematic quantitative proteomics. *Cell* 143: 951-965.
- 757 Berger, I, Fitzgerald, DJ, Richmond, TJ 2004. Baculovirus expression system for heterologous
758 multiprotein complexes. *Nat Biotechnol* 22: 1583-1587.
- 759 Birol, M, Enchev, RI, Padilla, A, Stengel, F, Aebersold, R, Betzi, S, Yang, Y, Hoh, F, Peter, M, Dumas, C,
760 et al. 2014. Structural and biochemical characterization of the Cop9 signalosome CSN5/CSN6
761 heterodimer. *PLoS One* 9: e105688.
- 762 Briggs, GE, Haldane, JB 1925. A Note on the Kinetics of Enzyme Action. *Biochem J* 19: 338-339.
- 763 Cope, GA, Deshaies, RJ 2006. Targeted silencing of Jab1/Csn5 in human cells downregulates SCF
764 activity through reduction of F-box protein levels. *BMC Biochem* 7: 1.
- 765 Cope, GA, Suh, GS, Aravind, L, Schwarz, SE, Zipursky, SL, Koonin, EV, Deshaies, RJ 2002. Role of
766 predicted metalloprotease motif of Jab1/Csn5 in cleavage of Nedd8 from Cul1. *Science* 298: 608-
767 611.
- 768 Cox, J, Mann, M 2008. MaxQuant enables high peptide identification rates, individualized p.p.b.-
769 range mass accuracies and proteome-wide protein quantification. *Nat Biotechnol* 26: 1367-1372.
- 770 Cox, J, Neuhauser, N, Michalski, A, Scheltema, RA, Olsen, JV, Mann, M 2011. Andromeda: a peptide
771 search engine integrated into the MaxQuant environment. *J Proteome Res* 10: 1794-1805.
- 772 den Besten, W, Verma, R, Kleiger, G, Oania, RS, Deshaies, RJ 2012. NEDD8 links cullin-RING
773 ubiquitin ligase function to the p97 pathway. *Nat Struct Mol Biol* 19: 511-516, S511.
- 774 Deshaies, RJ, Joazeiro, CA 2009. RING domain E3 ubiquitin ligases. *Annu Rev Biochem* 78: 399-434.
- 775 Dougherty, WG, Cary, SM, Parks, TD 1989. Molecular genetic analysis of a plant virus polyprotein
776 cleavage site: a model. *Virology* 171: 356-364.

- 777 Duda, DM, Borg, LA, Scott, DC, Hunt, HW, Hammel, M, Schulman, BA 2008. Structural insights into
778 NEDD8 activation of cullin-RING ligases: conformational control of conjugation. *Cell* 134: 995-
779 1006.
- 780 Echaliier, A, Pan, Y, Birol, M, Tavernier, N, Pintard, L, Hoh, F, Ebel, C, Galophe, N, Claret, FX, Dumas,
781 C 2013. Insights into the regulation of the human COP9 signalosome catalytic subunit, CSN5/Jab1.
782 *Proc Natl Acad Sci U S A* 110: 1273-1278.
- 783 Emberley, ED, Mosadeghi, R, Deshaies, RJ 2012. Deconjugation of Nedd8 from Cul1 is directly
784 regulated by Skp1-Fbox and substrate, and CSN inhibits deneddylated SCF by a non-catalytic
785 mechanism. *J Biol Chem*.
- 786 Enchev, RI, Schreiber, A, Beuron, F, Morris, EP 2010. Structural insights into the COP9 signalosome
787 and its common architecture with the 26S proteasome lid and eIF3. *Structure* 18: 518-527.
- 788 Enchev, RI, Schulman, BA, Peter, M 2015. Protein neddylation: beyond cullin-RING ligases. *Nat Rev*
789 *Mol Cell Biol* 16: 30-44.
- 790 Enchev, RI, Scott, DC, da Fonseca, PC, Schreiber, A, Monda, JK, Schulman, BA, Peter, M, Morris, EP
791 2012. Structural basis for a reciprocal regulation between SCF and CSN. *Cell reports* 2: 616-627.
- 792 Fischer, ES, Scrima, A, Bohm, K, Matsumoto, S, Lingaraju, GM, Faty, M, Yasuda, T, Cavadini, S,
793 Wakasugi, M, Hanaoka, F, et al. 2011. The Molecular Basis of CRL4(DDB2/CSA) Ubiquitin Ligase
794 Architecture, Targeting, and Activation. *Cell* 147: 1024-1039.
- 795 Kelley, LA, Mezulis, S, Yates, CM, Wass, MN, Sternberg, MJ 2015. The Phyre2 web portal for protein
796 modeling, prediction and analysis. *Nature protocols* 10: 845-858.
- 797 Leitner, A, Walzthoeni, T, Aebersold, R 2014. Lysine-specific chemical cross-linking of protein
798 complexes and identification of cross-linking sites using LC-MS/MS and the xQuest/xProphet
799 software pipeline. *Nature protocols* 9: 120-137.
- 800 Lingaraju, GM, Bunker, RD, Cavadini, S, Hess, D, Hassiepen, U, Renatus, M, Fisher, ES, Thoma, NH
801 2014. Crystal structure of the human COP9 signalosome. *Nature* 512: 161-165.
- 802 Liu, J, Furukawa, M, Matsumoto, T, Xiong, Y 2002. NEDD8 modification of CUL1 dissociates
803 p120(CAND1), an inhibitor of CUL1-SKP1 binding and SCF ligases. *Mol Cell* 10: 1511-1518.
- 804 Lyapina, S, Cope, G, Shevchenko, A, Serino, G, Tsuge, T, Zhou, C, Wolf, DA, Wei, N, Deshaies, RJ 2001.
805 Promotion of NEDD-CUL1 conjugate cleavage by COP9 signalosome. *Science* 292: 1382-1385.
- 806 Mindell, JA, Grigorieff, N 2003. Accurate determination of local defocus and specimen tilt in
807 electron microscopy. *J Struct Biol* 142: 334-347.
- 808 Orthwein 2015. Induction of homologous recombination in G1 cells. *Nature* in press.
- 809 Pettersen, EF, Goddard, TD, Huang, CC, Couch, GS, Greenblatt, DM, Meng, EC, Ferrin, TE 2004. UCSF
810 Chimera--a visualization system for exploratory research and analysis. *J Comput Chem* 25: 1605-
811 1612.
- 812 Pierce, NW, Lee, JE, Liu, X, Sweredoski, MJ, Graham, RL, Larimore, EA, Rome, M, Zheng, N, Clurman,
813 BE, Hess, S, et al. 2013. Cand1 promotes assembly of new SCF complexes through dynamic
814 exchange of F box proteins. *Cell* 153: 206-215.
- 815 Politis, A, Stengel, F, Hall, Z, Hernandez, H, Leitner, A, Walzthoeni, T, Robinson, CV, Aebersold, R
816 2014. A mass spectrometry-based hybrid method for structural modeling of protein complexes.
817 *Nat Methods* 11: 403-406.
- 818 Ritchie, ME, Phipson, B, Wu, D, Hu, Y, Law, CW, Shi, W, Smyth, GK 2015. limma powers differential
819 expression analyses for RNA-sequencing and microarray studies. *Nucleic Acids Res* 43: e47.
- 820 Rosenthal, PB, Henderson, R 2003. Optimal determination of particle orientation, absolute hand,
821 and contrast loss in single-particle electron cryomicroscopy. *J Mol Biol* 333: 721-745.
- 822 Saha, A, Deshaies, RJ 2008. Multimodal activation of ubiquitin ligase SCF by Nedd8 conjugation.
823 *Mol Cell* 32: 21-31.

- 824 Sato, Y, Yoshikawa, A, Yamagata, A, Mimura, H, Yamashita, M, Ookata, K, Nureki, O, Iwai, K, Komada,
825 M, Fukai, S 2008. Structural basis for specific cleavage of Lys 63-linked polyubiquitin chains.
826 *Nature* 455: 358-362.
- 827 Scheres, SH 2012. RELION: implementation of a Bayesian approach to cryo-EM structure
828 determination. *J Struct Biol* 180: 519-530.
- 829 Scheres, SH, Chen, S 2012. Prevention of overfitting in cryo-EM structure determination. *Nat*
830 *Methods* 9: 853-854.
- 831 Schmidt, MW, McQuary, PR, Wee, S, Hofmann, K, Wolf, DA 2009. F-box-directed CRL complex
832 assembly and regulation by the CSN and CAND1. *Mol Cell* 35: 586-597.
- 833 Shalem, O, Sanjana, NE, Hartenian, E, Shi, X, Scott, DA, Mikkelsen, TS, Heckl, D, Ebert, BL, Root, DE,
834 Doench, JG, et al. 2014a. Genome-scale CRISPR-Cas9 knockout screening in human cells. *Science*
835 343: 84-87.
- 836 Shalem, O, Sanjana, NE, Hartenian, E, Shi, X, Scott, DA, Mikkelsen, TS, Heckl, D, Ebert, BL, Root, DE,
837 Doench, JG, et al. 2014b. Genome-scale CRISPR-Cas9 knockout screening in human cells. *Science*
838 343: 3.
- 839 Skaar, JR, Pagan, JK, Pagano, M 2013. Mechanisms and function of substrate recruitment by F-box
840 proteins. *Nat Rev Mol Cell Biol* 14: 369-381.
- 841 Smyth, GK (2005). Limma: linear models for microarray data. In *Bioinformatics and computational*
842 *biology solutions using R and Bioconductor* (New York: Springer), pp. 397-420.
- 843 Soucy, TA, Smith, PG, Milhollen, MA, Berger, AJ, Gavin, JM, Adhikari, S, Brownell, JE, Burke, KE,
844 Cardin, DP, Cullis, CA 2009. An inhibitor of NEDD8-activating enzyme as a novel approach to treat
845 cancer. *Nature* 458: 732-736.
- 846 Suh, GS, Poeck, B, Chouard, T, Oron, E, Segal, D, Chamovitz, DA, Zipursky, SL 2002. Drosophila
847 JAB1/CSN5 acts in photoreceptor cells to induce glial cells. *Neuron* 33: 35-46.
- 848 Theile, CS, Witte, MD, Blom, AE, Kundrat, L, Ploegh, HL, Guimaraes, CP 2013. Site-specific N-
849 terminal labeling of proteins using sortase-mediated reactions. *Nature protocols* 8: 1800-1807.
- 850 Tran, HJ, Allen, MD, Lowe, J, Bycroft, M 2003. Structure of the Jab1/MPN domain and its
851 implications for proteasome function. *Biochemistry* 42: 11460-11465.
- 852 Wee, S, Geyer, RK, Toda, T, Wolf, DA 2005. CSN facilitates Cullin-RING ubiquitin ligase function by
853 counteracting autocatalytic adapter instability. *Nat Cell Biol* 7: 387-391.
- 854 Wu, S, Zhu, W, Nhan, T, Toth, JI, Petroski, MD, Wolf, DA 2013. CAND1 controls in vivo dynamics of
855 the cullin 1-RING ubiquitin ligase repertoire. *Nature communications* 4: 1642.
- 856 Yamoah, K, Oashi, T, Sarikas, A, Gazdoui, S, Osman, R, Pan, ZQ 2008. Autoinhibitory regulation of
857 SCF-mediated ubiquitination by human cullin 1's C-terminal tail. *Proc Natl Acad Sci U S A* 105:
858 12230-12235.
- 859 Zemla, A, Thomas, Y, Kedziora, S, Knebel, A, Wood, NT, Rabut, G, Kurz, T 2013. CSN- and CAND1-
860 dependent remodelling of the budding yeast SCF complex. *Nature communications* 4: 1641.
- 861 Zheng, N, Schulman, BA, Song, L, Miller, JJ, Jeffrey, PD, Wang, P, Chu, C, Koepp, DM, Elledge, SJ,
862 Pagano, M, et al. 2002. Structure of the Cul1-Rbx1-Skp1-F boxSkp2 SCF ubiquitin ligase complex.
863 *Nature* 416: 703-709.

864

865

866 **Figure Legends**

867 **Figure 1: Cryo-electron microscopy of a CSN-SCF complex.** (A) Molecular model of CSN^{5H138A}-
868 SCF-N8^{Skp2/Cks1} docked into the cryo-electron density map (gray mesh). (B) Close-up view of the
869 model, showing the observed conformations of Csn2, Csn4, Rbx1, Csn5/6 and WHB-Nedd8 and (C)
870 a cartoon representation of the differences between the apo CSN and substrate-bound state.

871 **Figure 2: Development and validation of a binding assay for CSN-Cul1/Rbx1 interaction.** (A)
872 Equilibrium binding of CSN to Cul1^d/Rbx1 and competition by unlabeled Cul1/Rbx1. The indicated
873 proteins were mixed and allowed to equilibrate prior to determination of dansyl fluorescence in a
874 fluorometer. Note that Cul1/Rbx1 blocks the fluorescence enhancement caused by CSN. CSN,
875 Cul1^d/Rbx1, and Cul1/Rbx1 were used at 350, 30, and 4000 nM, respectively. (B) Equilibrium
876 binding of CSN to Cul1^d/Rbx1. Cul1^d/Rbx1 (30 nM) was mixed with increasing concentrations of
877 CSN and the proteins were allowed to equilibrate prior to determining the change in dansyl
878 fluorescence in triplicate samples. Error bars represent standard deviation.

879 **Figure 3: Quantitative determination of enzyme-substrate binding affinities for wild type
880 and mutant proteins.** (A) Tight binding of CSN^{5H138A} to substrate. Cul1^d-N8/Rbx1 and CSN^{5H138A}
881 were mixed and allowed to equilibrate prior to determining the change in dansyl fluorescence. (B)
882 Summary of K_d measurements for the indicated CSN complexes tested against unmodified
883 Cul1^d/Rbx1, Nedd8-conjugated Cul1^d-N8/Rbx1 or Cul1^d-N8/Rbx1^{ΔRING} ligand. Boxes shaded in
884 gray indicate combinations that could not be analyzed due to deneddylation during the binding
885 reaction. For some complexes that bound weakly it was not feasible to titrate to saturation and so
886 a lower boundary for K_d is indicated. N.D., not determined. *, due to the configuration of our assay,
887 extremely low K_d values cannot be reliably determined. (C) Summary of k_{on} and k_{off} measurements
888 for the indicated CSN complexes tested against Cul1^d/Rbx1 or Cul1^d-N8/Rbx1. Each reported k_{off} is
889 the mean of at least 8 replicates. For comparison, k_{off} values calculated from k_{on} and K_d
890 measurements are also shown. For cases where k_{on} was not measured (marked with asterisks),
891 we assumed a value that was the average ($1.83 \times 10^7 \text{ M}^{-1} \text{ sec}^{-1}$) of the three measured k_{on} values.
892 Boxes shaded in gray indicate combinations that could not be analyzed due to deneddylation upon
893 complex formation. N.D., not determined.

894 **Figure 4: The N-terminal domains of Csn2 and Csn4 and the RING domain of Rbx1 play key
895 roles in substrate binding and deneddylation.** (A) Generation of Cul1-N8/Rbx1^{ΔRING}. Top: a TEV
896 protease site was engineered between the N-terminal β -strand and the RING domain of Rbx1 as

897 indicated. Only the first 50 amino acids of Rbx1 are shown. Bottom: Purified protein was subjected
898 to the indicated treatments (see Materials and Methods for details) and reactions were
899 fractionated by SDS-PAGE and stained with Coomassie Blue. (B) Deletion of the Csn4-NTD and
900 Rbx1-RING domains independently reduce affinity of CSN for substrate. The indicated proteins
901 were mixed and allowed to equilibrate prior to determining the change in dansyl fluorescence in
902 triplicate samples. Error bars represent standard deviation. K_d values measured in this experiment
903 are also reported in Figure 3B.

904 **Figure 5: The N-terminal domains of Csn2 and Csn4 and the RING domain of Rbx1 are**
905 **important for CSN-mediated deneddylation.** (A) Summary of kinetic parameters for the
906 indicated CSN mutants in multi- or single-turnover deneddylation reactions with Cul1-N8/Rbx1 or
907 Cul1-N8/Rbx1^{ΔRING} substrate. Note that there may be modest discrepancies between these k_{cat}
908 values and k_{off} values due to differences in assay configurations as described in Materials and
909 Methods. The ΔRING substrate used here and in panel B contains the sortase sequence at the C-
910 terminus of Cul1 that was used for generation of dansylated Cul1. Control experiments revealed
911 that this tag, with or without dansylation, reduced k_{cat} by ~4-fold. In addition the wild type control
912 for the ΔRING reaction exhibited k_{cat} of 2.6 sec⁻¹. The rates shown have been correspondingly
913 adjusted to normalize them to other rates reported here. *, This rate is estimated from Figure 5-
914 figure supplement 5B. (B) Kinetic analysis of deneddylation of Cul1-N8/Rbx1^{ΔRING} by CSN.

915 **Figure 6: Functional analysis of Csn5 active site and INS1 mutants in biochemical and**
916 **cellular assays.** (A) Csn5-E104 is important for CSN function in cells. *CSN5* alleles in HEK293T
917 cells were partially knocked out (KO) by CRISPR/Cas9 to yield a major decrease in Csn5 that was
918 nonetheless compatible with viability. Wild type and the indicated Flag-tagged *CSN5* mutants were
919 reintroduced by transduction of recombinant retroviruses that co-expressed GFP. Lysates of
920 transduced cells were separated by SDS-PAGE and blotted with antibodies to the indicated
921 proteins. CSN5 long refers to a long exposure of the Csn5 blot, captured to reveal residual Csn5 in
922 the knock-out cells. # refers to transduced FlagCsn5 and * refers to endogenous Csn5. (B) Any
923 mutation of a core JAMM domain residue in Csn5 results in enhanced binding to Cul1. Same as (A),
924 except additional Csn5 mutants were tested and the cell lysates were immunoprecipitated with
925 anti-Flag and the immunoprecipitates were blotted for the indicated proteins. (C) Csn5-T103 is
926 important for CSN function in cells. Same as (A) except that the Csn5-T103I mutant was analyzed
927 in parallel with Csn5-E104A and wild type. (D) SILAC mass spectrometry of endogenous proteins

928 bound to ^{Flag}Csn5-E104A or ^{Flag}Csn5-T103I, relative to wild type ^{Flag}Csn5. Cells expressing mutant
929 and wild type ^{Flag}Csn5 proteins were grown in light and heavy medium, respectively. L:H ratios >1
930 indicate higher recovery of the listed protein from cells expressing mutant ^{Flag}Csn5, whereas ratios
931 <1 indicate higher recovery from cells expressing wild type ^{Flag}Csn5. Gray bars: ^{Flag}Csn5-E104A;
932 black bars: ^{Flag}Csn5-T103I. Error bars represent the 95% confidence interval as calculated by
933 limma (Smyth, 2005). Each protein was quantified in at least two of the four biological replicates
934 and error bars represent standard deviations. Ratios indicated by * differed significantly from 1.0
935 ($p < 0.05$). For CSN, only Csn5 is shown; the remainder is shown in Figure 6–figure supplement 6B.

936 **Figure 7: Structural and kinetic models for CSN activation and the CSN enzyme cycle.** (A-C)
937 Proposed conformational changes that precede substrate cleavage. (D) Kinetic model for the
938 deneddylation cycle. Substrate cleavage is indicated by the slash between N8 and SCF. The asterisk
939 denotes the activated form of CSN. Numbers in red, black, green, and blue represent k_{off} (sec^{-1}), k_{on}
940 ($\text{M}^{-1} \text{sec}^{-1}$), k_{cat} (sec^{-1}), and conformational change (sec^{-1}) rates, respectively. For rates >1, the
941 actual rate has not been measured but it is inferred to be $>1 \text{ sec}^{-1}$ because the overall rate for
942 multiturnover catalysis is at least 1.1 sec^{-1} and thus all sub-steps must be at least this fast. The k_{off}
943 of SCF from CSN varied depending upon whether the rate was measured directly or inferred from
944 K_d and k_{on} (see Fig. 3C). The arrow connecting CSN and N8-SCF•CSN* combines two separate
945 steps: binding of N8-SCF to CSN, and activation of CSN to CSN*.

946 **Figure 1–figure supplement 1: Cryo-electron microscopy and single particle analysis of a**
947 **CSN^{5H138A}-N8-SCF^{Skp2/Cks1} complex.** (A) A representative cryo-electron micrograph of a
948 CSN^{5H138A}-N8-SCF^{Skp2/Cks1} complex with some single molecular views indicated by white circles
949 (left) and a power spectrum indicating Thon rings reaching 6 \AA (right). Scale bar is 200 \AA . (B)
950 Representative two-dimensional class averages from the curated dataset, used for the subsequent
951 analysis. Scale bar is as in (A). (C) Surface views of the final, post-processed cryo-electron map. (D).
952 Resolution estimate according to the FSC criteria of 0.143 and 0.5. (E) Fit of the PCI-domain
953 containing CSN subunits in the cryo-electron density map. Csn1,3,7, and 8 match the density very
954 well but the N-terminal domains of Csn2 and Csn4 do not, but their winged-helix domains fit well.
955 The horseshoe arrangement of the six winged-helix domains is indicated with a dotted black line.
956 (F) All the C-terminal helices of the CSN subunits match well the electron density map. (G) Fit of
957 SCF in the electron density map. (H) Same view as in Fig 1B but prior to flexible docking of the N-
958 terminal domains of Csn2 and Csn4, the MPN domains of Csn5&6, the WHB domain of Cul1, and

959 Nedd8. (I) Movement of the N-terminus of Csn2 from its crystallographically-determined position
960 (left) into the EM density map (right). (J) Movement of the N-terminus of Csn4 from its
961 crystallographically-determined position (left) into the EM density map (right). The two N-
962 terminal helical repeats of Csn4, red arrow, are in close proximity to the WHA domain of Cul1
963 (green circle). (K) Localization of the RING domain of Rbx1. The unfilled density that is indicated
964 by a black ellipse in the right-hand panel of S1J accommodates Rbx1 (shown in red). The helices of
965 Csn4 in close proximity to the RING domain of Rbx1 are indicated by a black arrow. (L) Re-
966 localization of Csn5/6. Comparing the left and right panels, Csn5/6 move leftward to occupy
967 unfilled density. The tan and green circles below Csn5/6 indicate densities that are occupied by
968 Nedd8 and the WHB domain, as depicted in (M). (N, O) Deneddylation assays with (N) wild type
969 Cul1-N8/Rbx1 and indicated CSN variants and (O) wild type CSN and mutant Cul1 variants. Note
970 that all Cul1 constructs have an uncleaved C-terminal sortase tag, which is the reason for slower
971 deneddylation of wild type Cul1-N8/Rbx1 by wild type CSN relative to the kinetics reported
972 elsewhere in this work.

973 **Figure 2-figure supplement 1: Supporting data for development and validation of CSN-**
974 **Cul1^d/Rbx1 binding assay.** (A) Dansylation of Cul1/Rbx1 constructs. Upper panel: dansylation of
975 bacterially expressed and purified Cul1/Rbx1. Lower panel: dansylation of Cul1/Rbx1 expressed
976 and purified from insect cells. For details, see Materials and Methods. (B) Ubiquitination of ³²P-
977 labeled β -catenin substrate peptide by dansylated SCF ^{β -TrCP} was monitored as described (Saha and
978 Deshaies, 2008). The k_{cat} measured here (0.048 min⁻¹) compares favorably with that previously
979 determined for wild type unmodified SCF (0.054 min⁻¹) (Saha and Deshaies, 2008). (C) IC₅₀ study
980 of the inhibitory effects of unlabeled (red) or dansylated (black) product. Cul1/Rbx1 and
981 Cul1^d/Rbx1 were separately titrated into a deneddylation reactions containing 50 nM Cul1-
982 [³²P]N8/Rbx1 substrate and 0.5 nM CSN, and the resulting reaction rate was measured. (D) CSN
983 preparations used in this study. 600 ng of each sample were fractionated by SDS-PAGE and stained
984 with SYPRO Ruby. (E) IC₅₀ for competitive inhibition of CSN-Cul1^d/Rbx1 complex formation by
985 unlabeled Cul1/Rbx1 (~ 390 nM) agrees with the K_d measured for binding of Cul1^d/Rbx1 to CSN
986 (310 nM). (F) Equilibrium binding of 100 nM CSN to 50 nM Cul1^d/Rbx1 and competition by 500
987 nM Cand1. The indicated proteins were mixed and allowed to equilibrate prior to determination of
988 dansyl fluorescence. (G-I) Free Nedd8 and F-box box proteins do not appreciably change affinity of
989 Cul1^d/Rbx1 for CSN. Same as Figure 2C, except that either 5 μ M free Nedd8 (G), 100 nM

990 Skp2/Skp1 (H) or 100 nM Fbxw7/Skp1 (I) was included in the binding reaction. All binding and
991 activity measurements reported in this legend were carried out in triplicate and error bars
992 represent standard deviation.

993 **Figure 3–figure supplement 1: Supporting experiments and titration curves for binding**
994 **data in Figures 3B–C.** (A) CSN^{5H138A} is inactive and is a dominant-negative inhibitor of
995 neddylation. CSN, CSN^{5H138A}, and substrate were used at 2 nM, 100 nM, and 75 nM, respectively.
996 For reactions containing with CSN and CSN^{5H138A}, mutant enzyme was preincubated with substrate
997 for 30 sec prior to initiating time-course by adding CSN. (B–E): The indicated proteins were mixed
998 and allowed to equilibrate prior to determining the change in dansyl fluorescence. (B) CSN^{5H138A}
999 and dansylated, Nedd8-conjugated SCF^{Skp2}. (C) CSN^{5H138A} and dansylated, Nedd8-conjugated
1000 SCF^{Fbxw7}. Note that addition of Fbxw7–Skp1 greatly increased the variability in the measurement
1001 for unknown reasons. (D) CSN^{5H138A} (first prep) and Cul1^d/Rbx1, (E) CSN^{5H138A} (second prep) and
1002 Cul1^d/Rbx1, (F–I): The indicated CSN complexes were preincubated with Cul1^d/Rbx1 for 10 min,
1003 followed by addition of unlabeled Cul1/Rbx1 chase and measurement of the decay in dansyl
1004 fluorescence over time. Final protein concentrations are listed for each experiment. (F) CSN (2000
1005 nM), Cul1^d/Rbx1 (200 nM), and Cul1/Rbx1 (3000 nM), (G) CSN^{5E104A} (600 nM), Cul1^d/Rbx1 (200
1006 nM), and Cul1/Rbx1 (3000 nM), (H) CSN^{5E76A,5H138A} (400 nM), Cul1^d/Rbx1 (200 nM), and
1007 Cul1/Rbx1 (3000 nM), (I) CSN^{5E76A,5H138A} (200 nM), Cul1^d-N8/Rbx1 (100 nM), and Cul1/Rbx1
1008 (1500 nM), (J–S): The indicated proteins were mixed and allowed to equilibrate prior to
1009 determining the change in dansyl fluorescence. (J) CSN^{5E76A,5H138A} and Cul1^d/Rbx1, (K) CSN^{5H138A}
1010 or CSN^{2ΔN,5H138A} and Cul1^d-N8/Rbx1, (L) CSN^{4ΔN,5H138A} and Cul1^d/Rbx1, (M) CSN^{4ΔN,5H138A} and
1011 Cul1^d-N8/Rbx1, (N) CSN^{5E76A} or CSN^{5E76A,5H138A} and Cul1^d-N8/Rbx1^{ΔRING}, (O) CSN^{5E104A} and
1012 Cul1^d/Rbx1, (P) CSN^{5E76A} and Cul1^d/Rbx1, (Q) CSN^{5H138A,6ΔINS2} and Cul1^d/Rbx1, (R) CSN^{5H138A,6ΔINS2}
1013 and Cul1^d-N8/Rbx1^{ΔRING}, (S) CSN^{5T103I} and Cul1^d/Rbx1. All measurements in panels B–E and J–S
1014 were carried out in triplicate and error bars represent standard deviation. The measurement in
1015 panel P was performed in duplicates but the experiment was repeated on three independent
1016 occasions, obtaining similar results. Several of these results were independently confirmed in
1017 Zurich and Pasadena including panels J, M, O, P, and Q.

1018 **Figure 4–figure supplement 1: Biochemical characterization of Cul1/Rbx1^{TEVΔRING} proteins.**
1019 (A) Ubiquitination assay using the indicated Cul1-N8/Rbx1 variants (500 nM each) as an E3. Each
1020 reaction contained, in addition, 100 nM Ube1, 1000 nM Cdc34b, 750 nM Skp1/Fbxw7 and 4000

1021 nM CyclinE phosphopeptide, labeled with FAM. The samples were incubated at 25°C for the
1022 indicated time points, analyzed by SDS PAGE and visualized by excitation at 473 nm. (B) Overlay
1023 of Superdex 200 size exclusion profiles of purified Cul1/Rbx1 variants isolated from insect cells.

1024 **Figure 5–figure supplement 1: Kinetic analysis of deneddylation.** (A) Deneddylation reactions
1025 were carried out in triplicate with CSN^{4ΔN} at varying concentrations of Cul1-[³²P]N8/Rbx1
1026 substrate and quantified to generate the curve shown. Estimates of k_{cat} and K_M are indicated. (B)
1027 Deneddylation assays of Cul1-N8/Rbx1^{ΔRING} (100 nM), incubated with CSN (200 nM, upper panel)
1028 or CSN^{6ΔINS2} (200 nM, lower panel). Samples were taken at the indicated time points, and
1029 visualized by SDS PAGE and Sypro Ruby staining. Note that the ΔRING substrate contained an
1030 unreacted Sortase tag at the C-terminus of Cul1 that reduced k_{cat} by ~4-fold. (C) Multi-turnover
1031 deneddylation reactions were carried out with CSN or CSN^{5E104A} and Cul1-[³²P]N8/Rbx1.
1032 Substrate was assayed at 1 and 1.3 μM to confirm that saturation was achieved. (D) Single-
1033 turnover deneddylation reactions were carried out with CSN on Cul1-[³²P]N8/Rbx1 +/-
1034 Skp1/Skp2, and with CSN^{5E104A} on Cul1-[³²P]N8/Rbx1. (E) Same as panel D except that CSN^{6ΔINS2}
1035 was also evaluated. (F) Multi-turnover deneddylation reactions were carried out in triplicate with
1036 CSN^{5T103I} at varying concentrations of Cul1-[³²P]N8/Rbx1 substrate and quantified to generate the
1037 curve shown. Estimates of k_{cat} and K_M are indicated.

1038 **Figure 6–figure supplement 1: Time course and titration data for Figure 6A and**
1039 **supplementary immunoblot for Figure 6B.** (A) Same as Figure 6B except that samples were
1040 immunoblotted for different cullins. (B) SILAC data for CSN subunits from pull-down analysis
1041 shown in Figure 6D.

1042 **Supplementary File 1: Table S1. Cross-links within CSN^{5H138A}-SCF-N8^{Skp2/Cks1}.** "Id" gives the
1043 amino acid sequence of the cross-linked peptides and the exact position of the two cross-linked
1044 lysine residues is indicated by the numbers of the letters *a* and *b* respectively for the first and
1045 second peptide. "Protein1" and "Protein2" denote the cross-linked protein names and "Residue
1046 1" and "Residue 2" respectively defines the position of the cross-linked lysine within the
1047 sequence of the protein. "deltaS" is the delta score of the respective cross-link, which serves as a
1048 measure for how close the best assigned hit was scored in regard to the second best. "Id_Score" is
1049 a weighted sum of four subscores: xcorr, xcorr_x, match-odds and TIC that is used to assess the
1050 quality of the composite MS2 spectrum as calculated by *xQuest*. "FDR" denotes the false-discovery

1051 rate as calculated by *xProphet*. The measured distance in Å is given for all cross-links, which fall
1052 within modeled residues.

1053 **Table S2. Cross-links within CSN5^{H138A}-SCFSkp2/Cks1**

1054 **Table S3. Cross-links within CSN-Cul1/Rbx1**

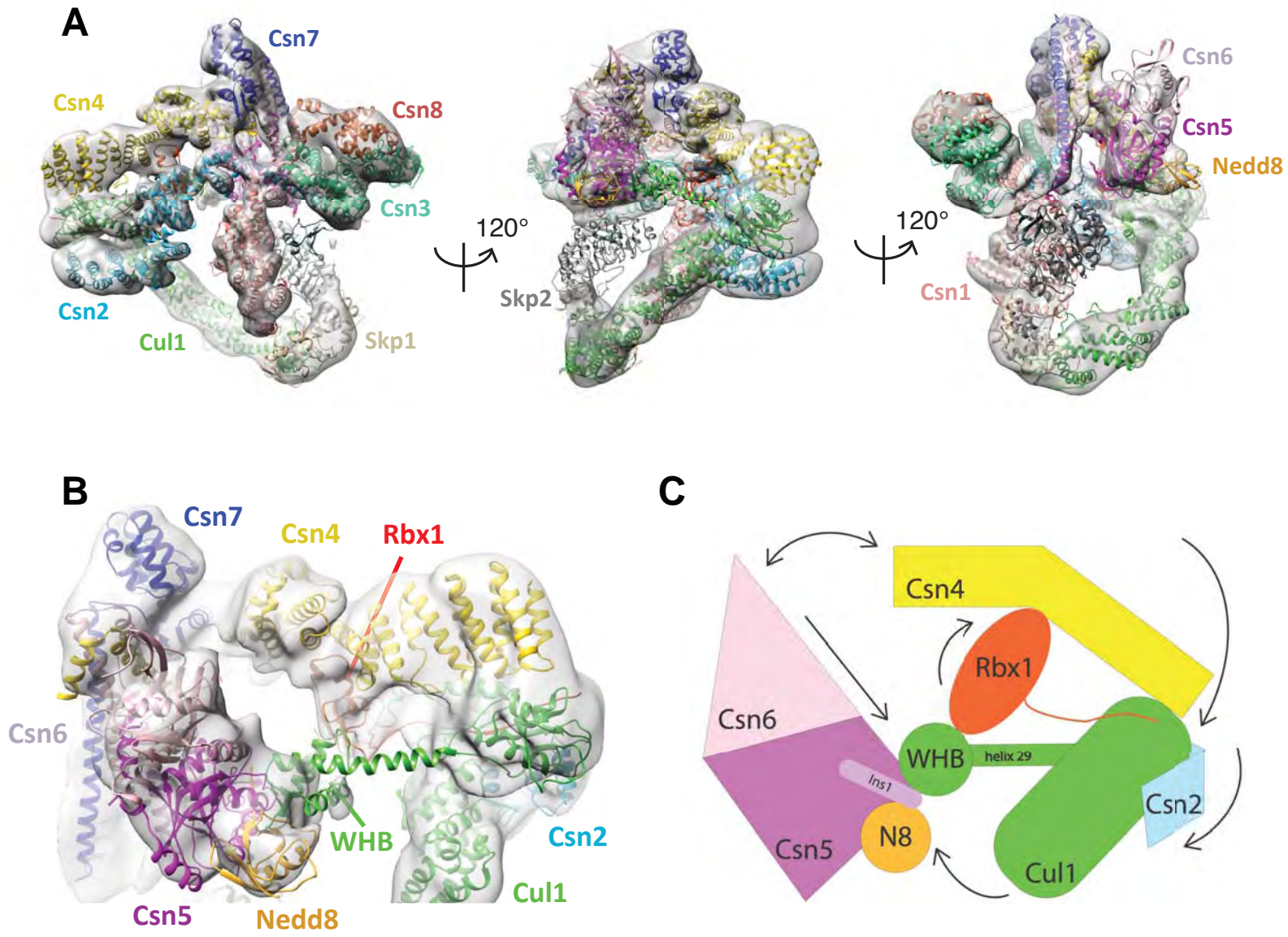
1055 **Table S4. Cross-links within CSN- SCF-N8^{Fbxw7FL}**

1056 **Table S5. Cross-links within CSN- SCF-N8^{Fbxw7trunc}**

1057 **Table S6. Cross-links within CSN- Cul3/Rbx1**

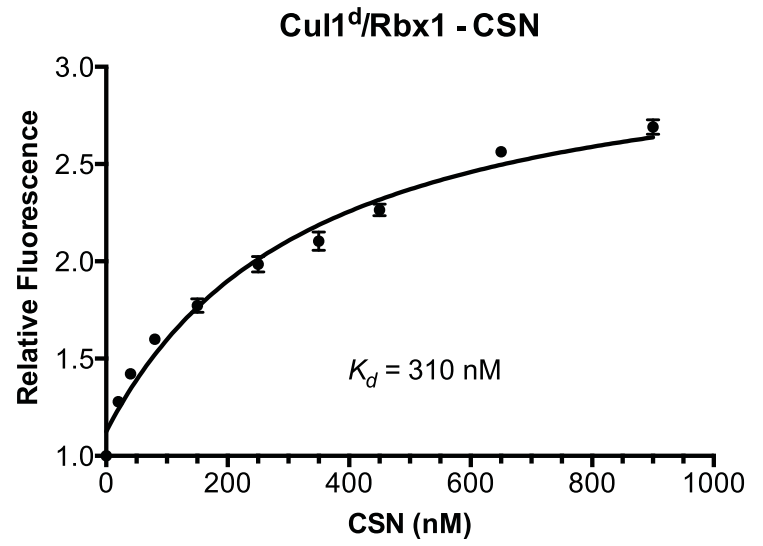
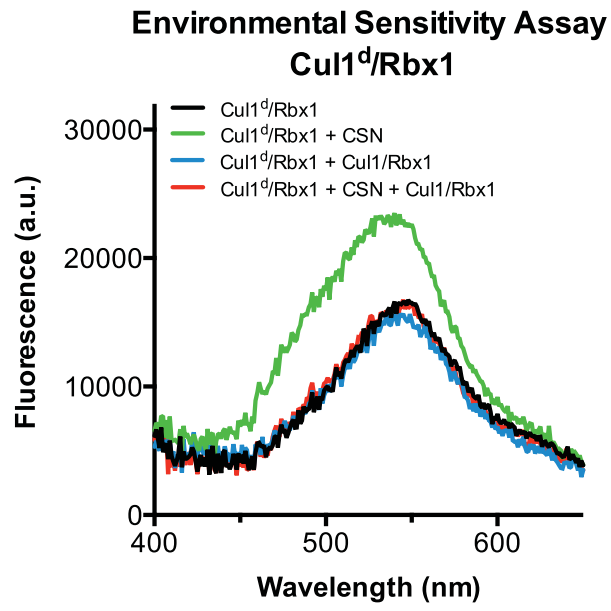
1058 **Movie 1: Morphing CSN and Cul1-N8/Rbx1 conformational changes, occurring upon binding.**
1059 Color code as in Figure 1.

1060



2A

2B



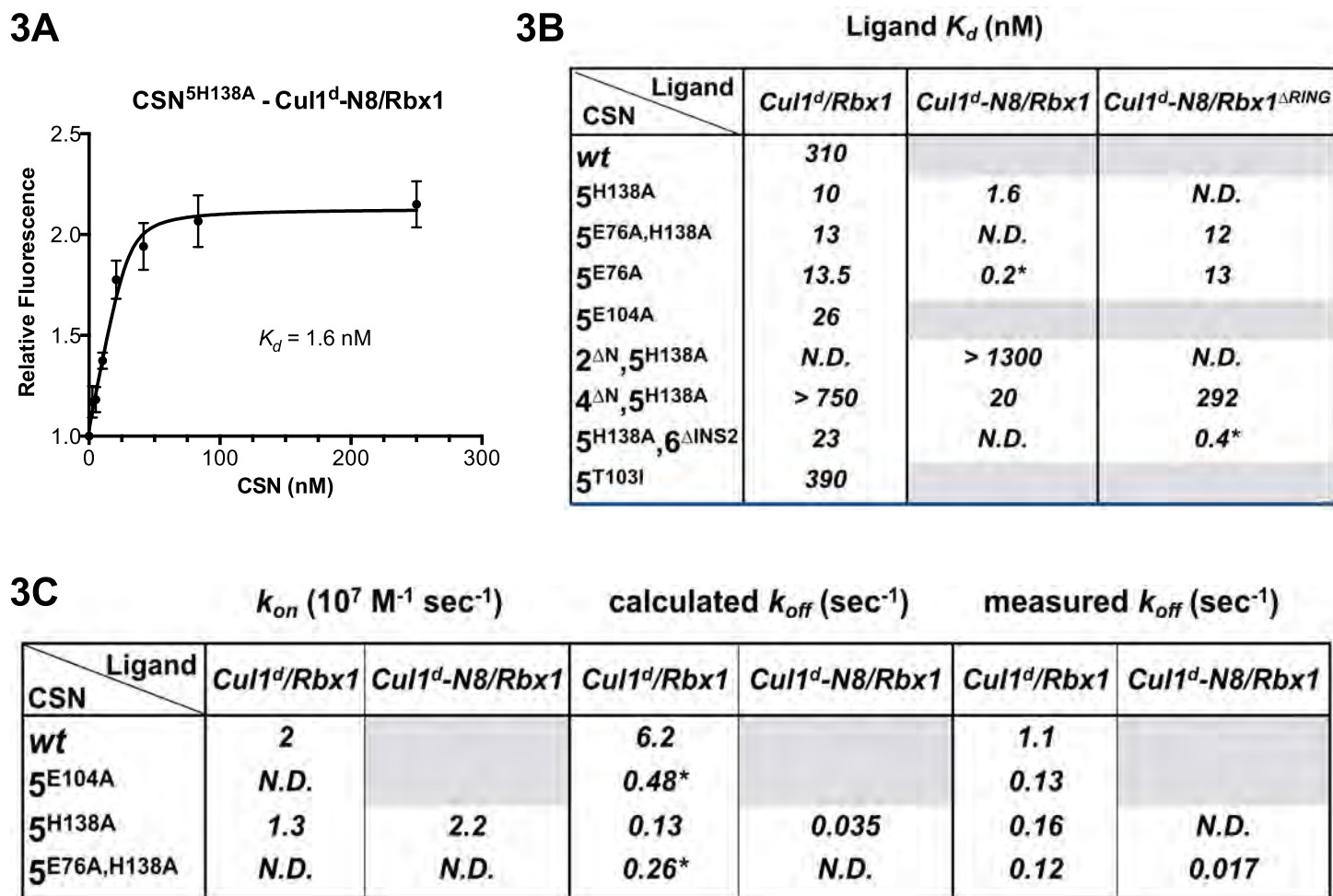
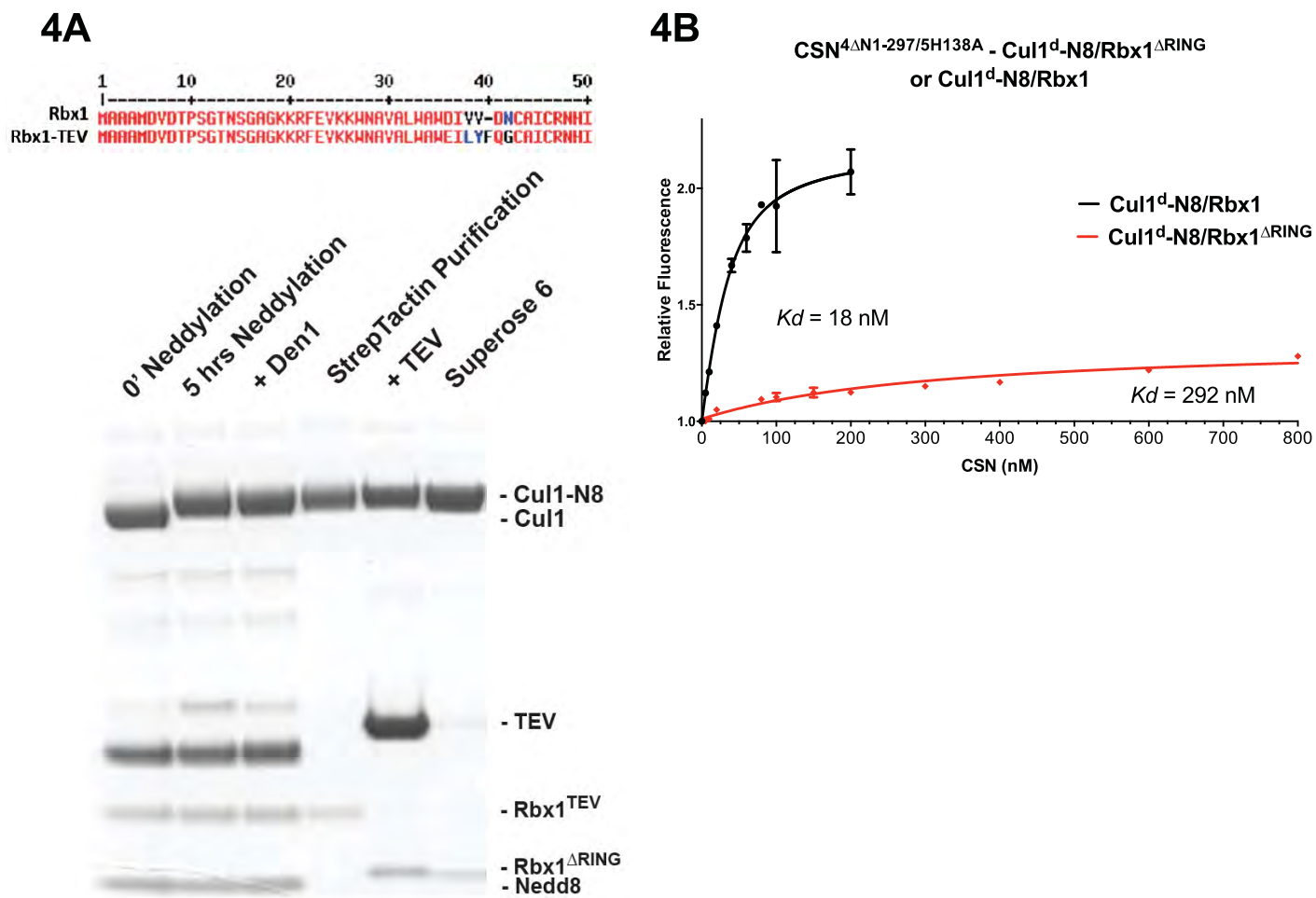


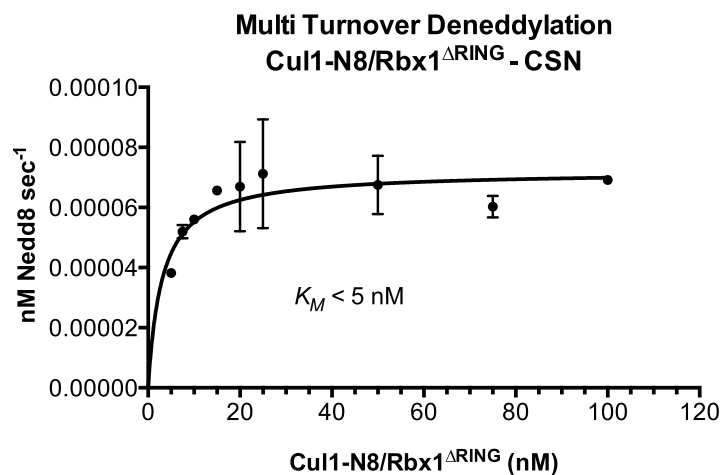
Figure 4

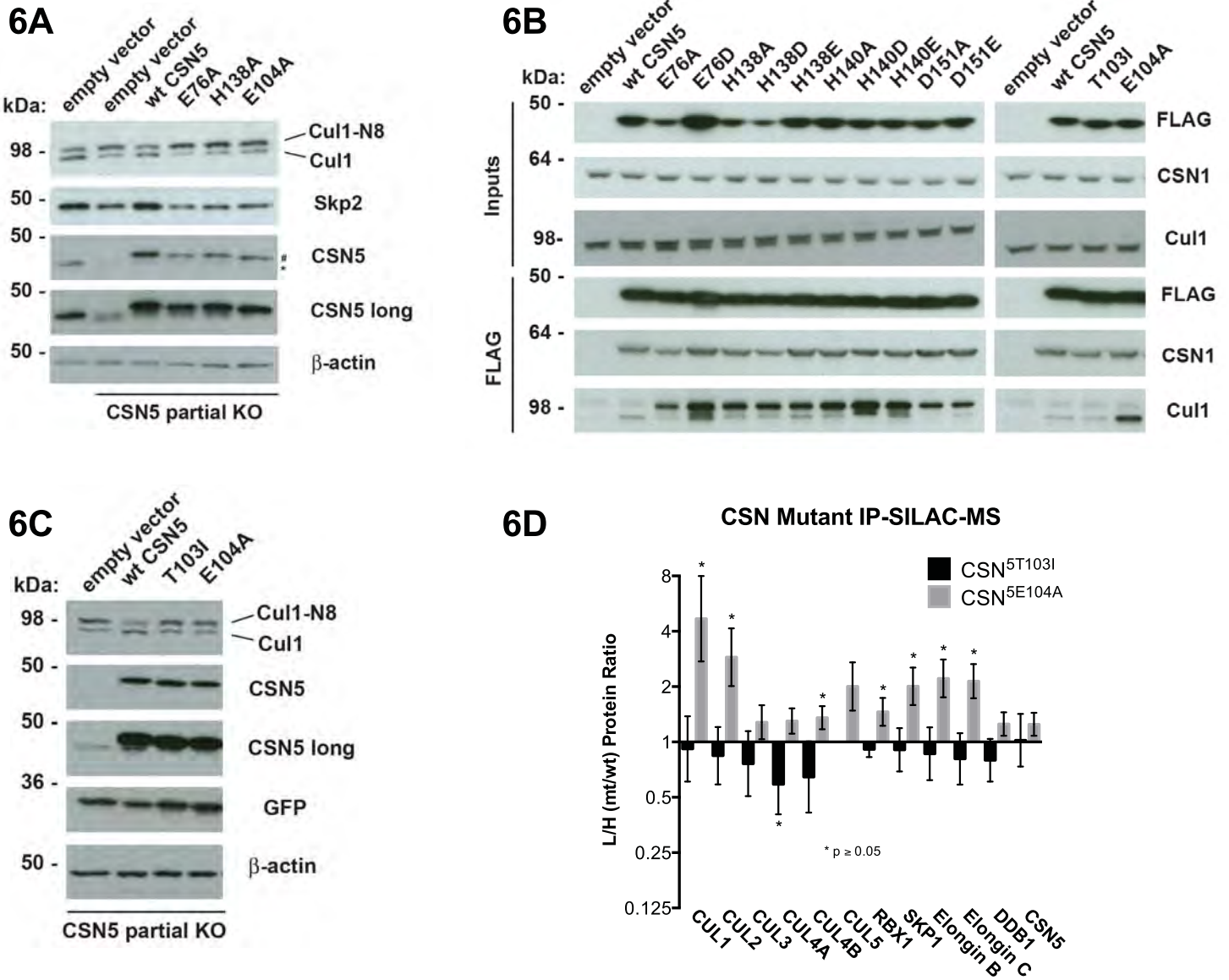


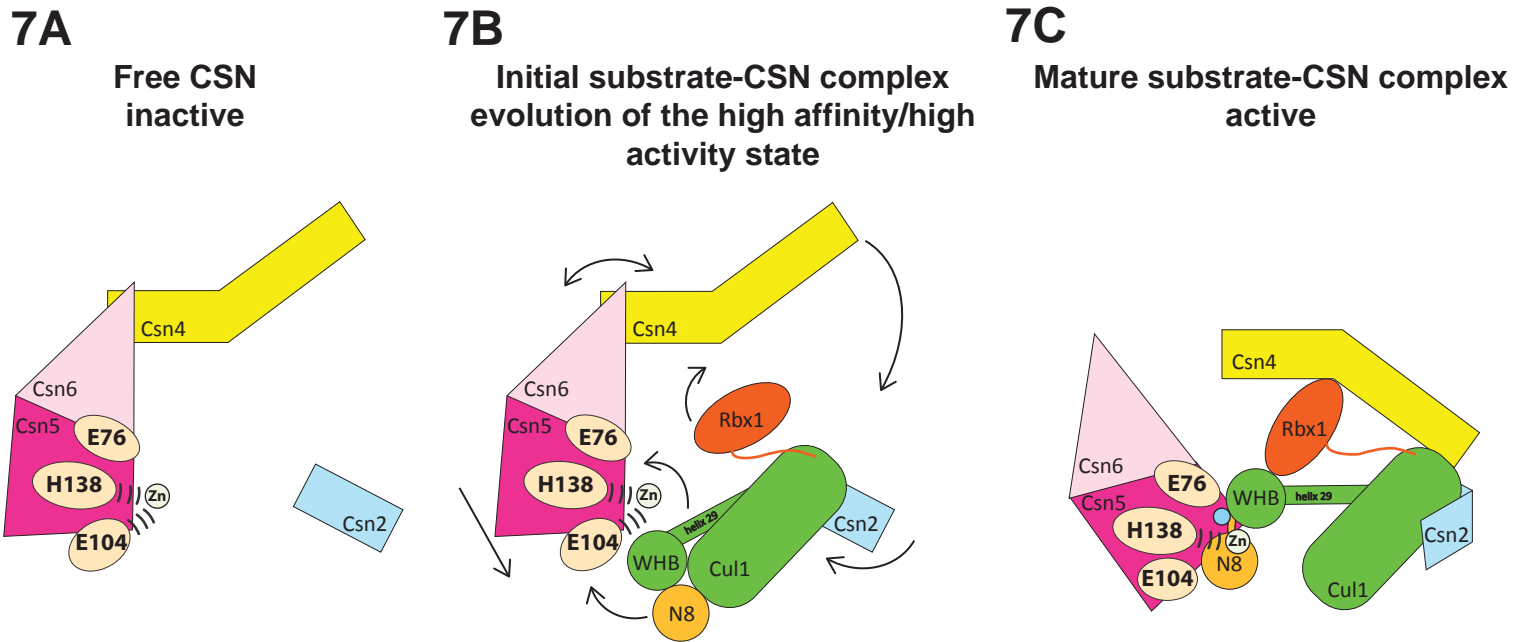
5A

CSN	k_{cat} (sec ⁻¹)	K_M (nM)	k_{cat} (sec ⁻¹)	k_{cat} (sec ⁻¹)
<i>wt</i>	1.1	200	1.1	0.00006
4 Δ N	0.05	40	N.D.	N.D.
6 Δ INS2	N.D.	N.D.	1.7	0.00048*
5 ^{E104A}	0.4	N.D.	0.4	N.D.
5 ^{T103I}	≤ 0.09	90	N.D.	N.D.
turnover	<i>multi</i>		<i>single</i>	<i>multi</i>
substrate	<i>Cul1-N8/Rbx1</i>			<i>Cul1-N8/Rbx1</i> ^{ΔRING}

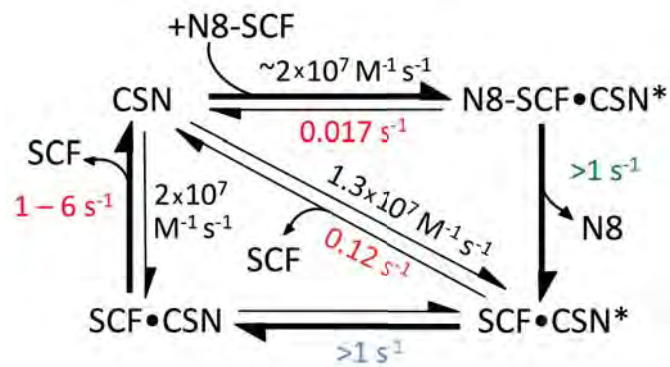
5B



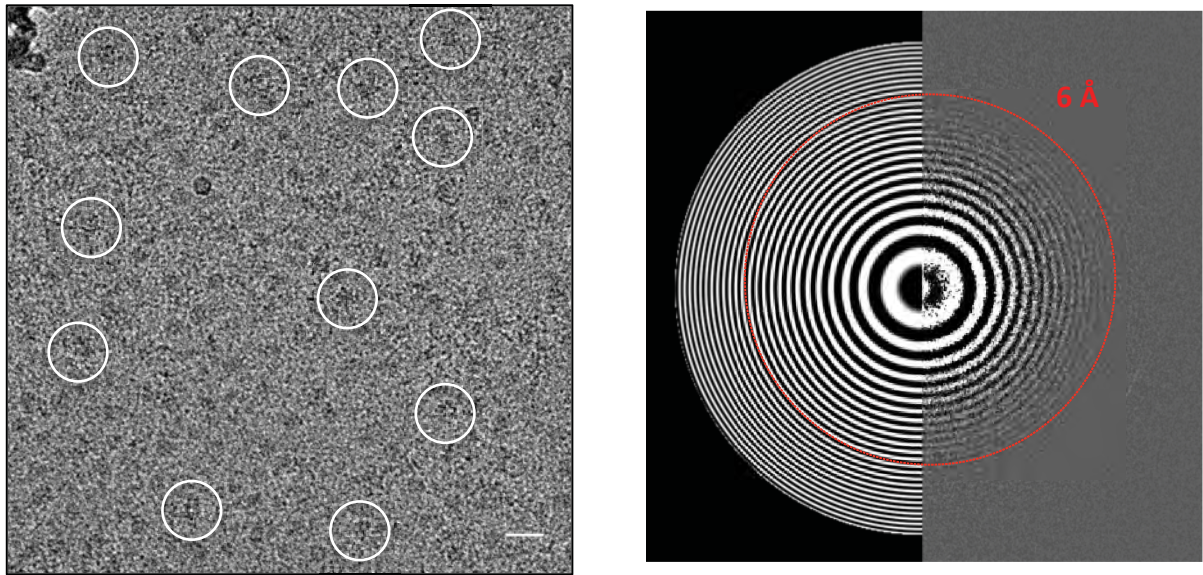




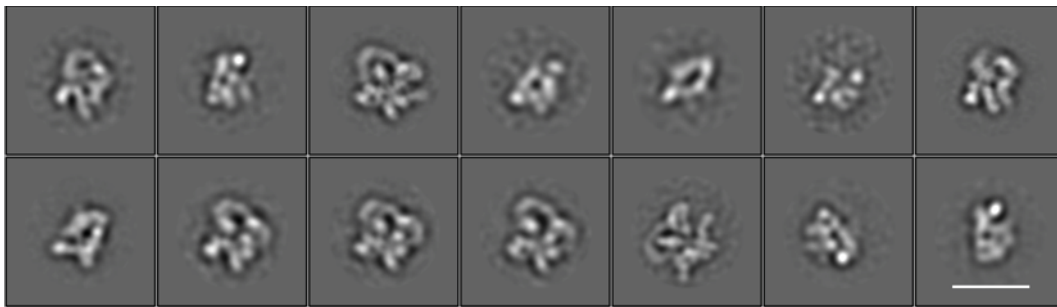
7D



S1A



S1B



S1C

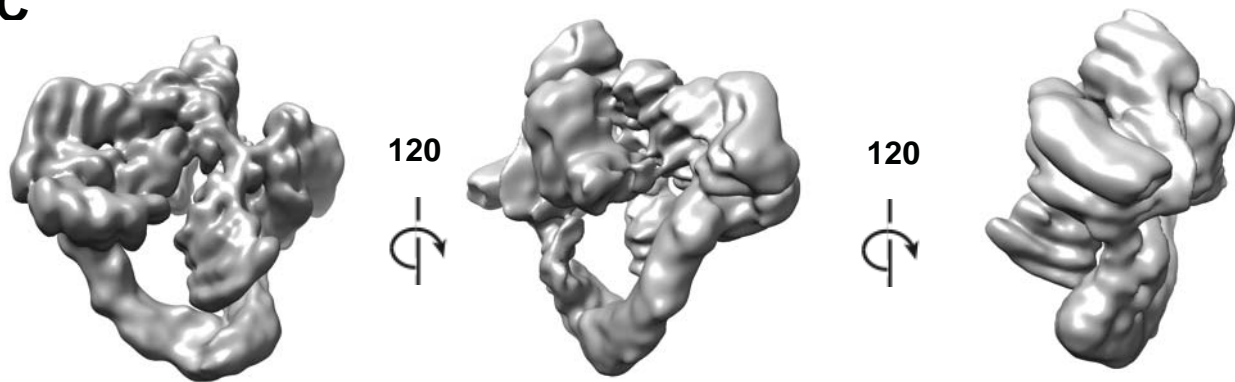
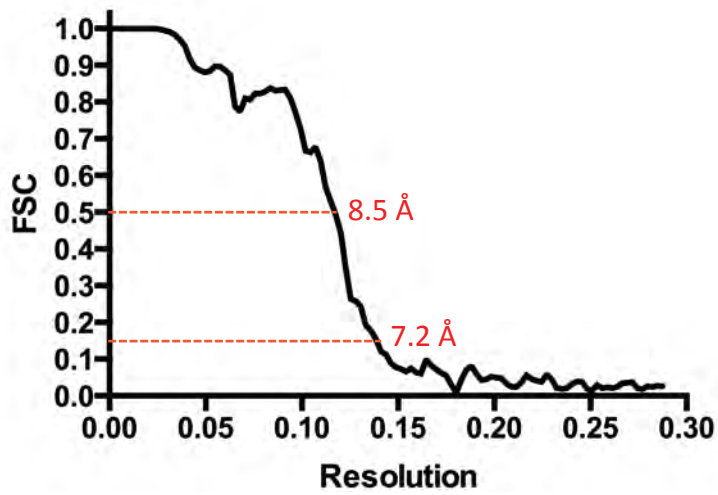
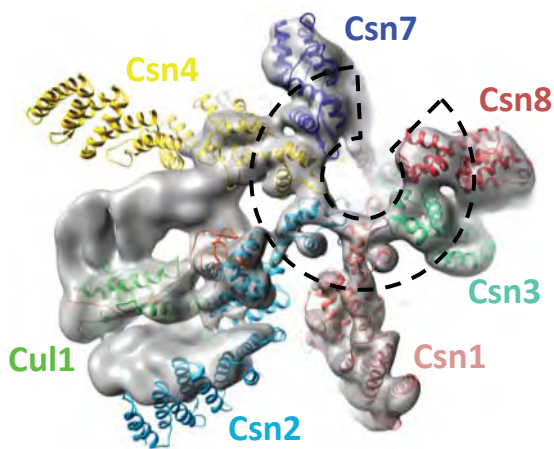


Figure Supplement 1

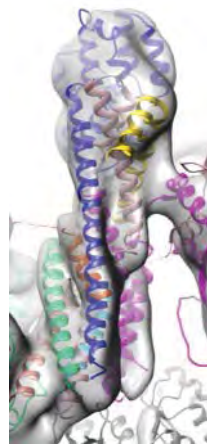
S1D



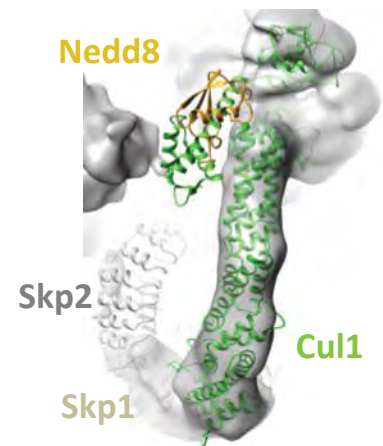
S1E



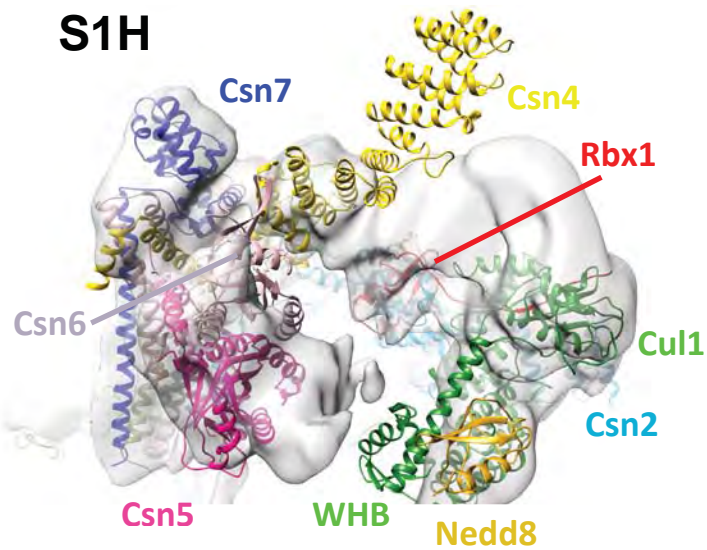
S1F



S1G



S1H



S1I

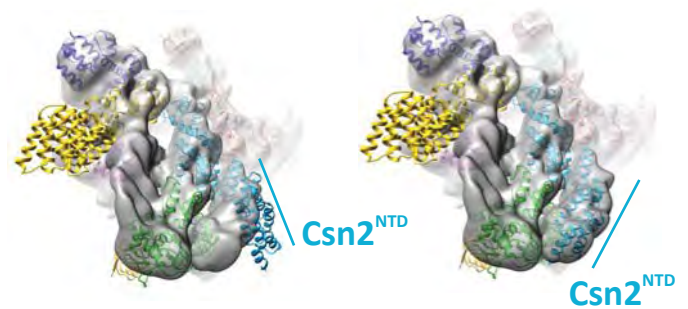


Figure Supplement 1

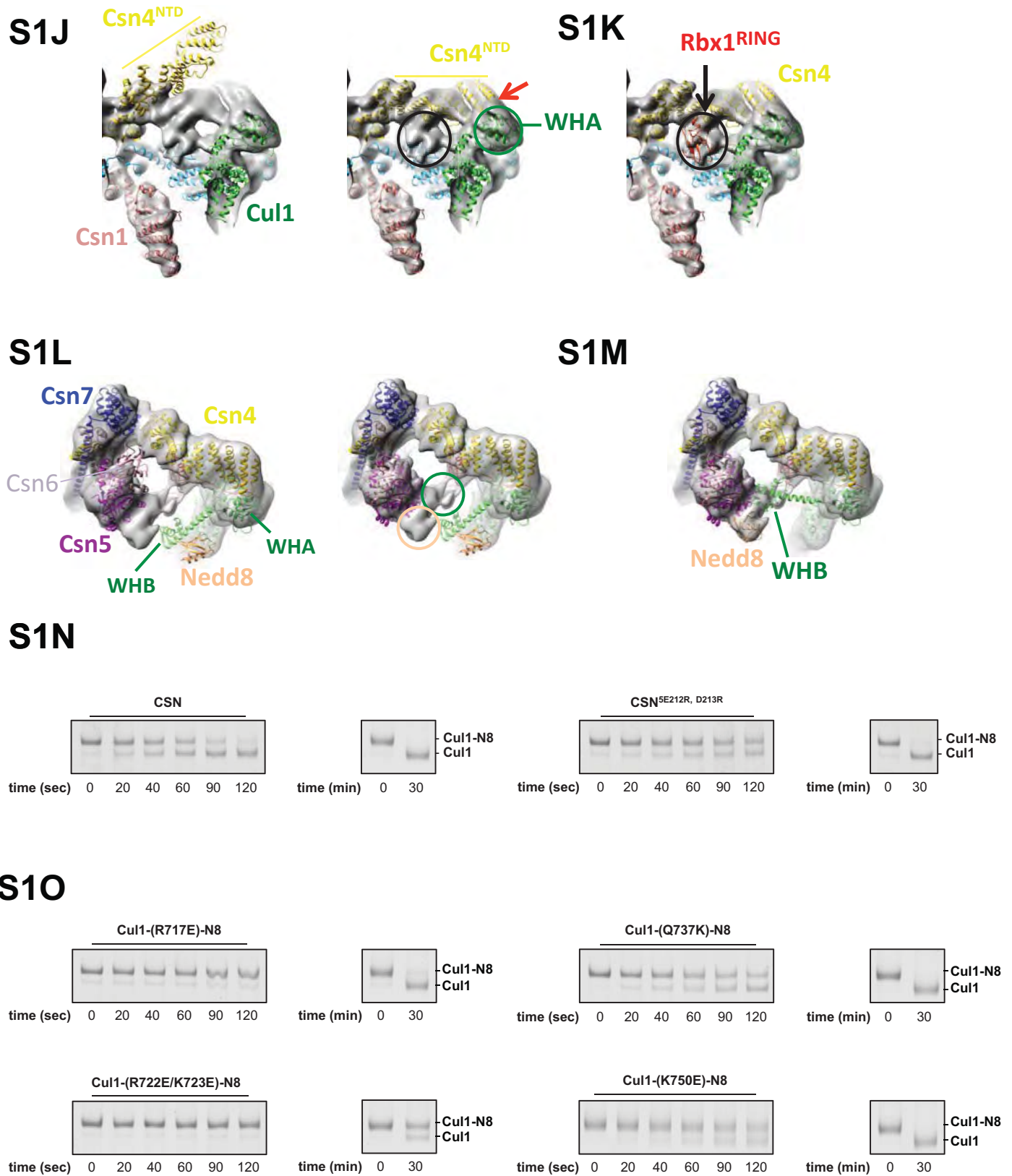
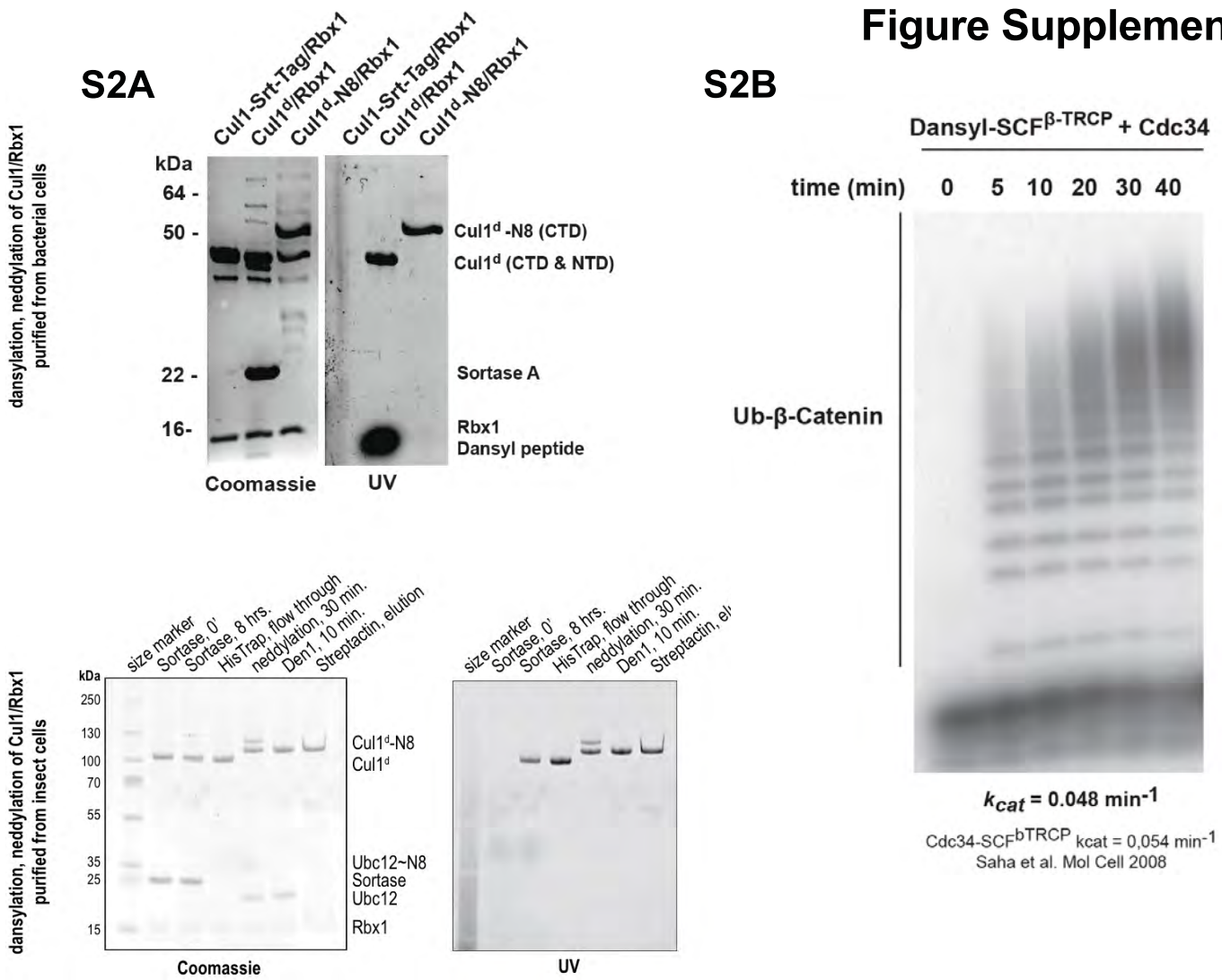
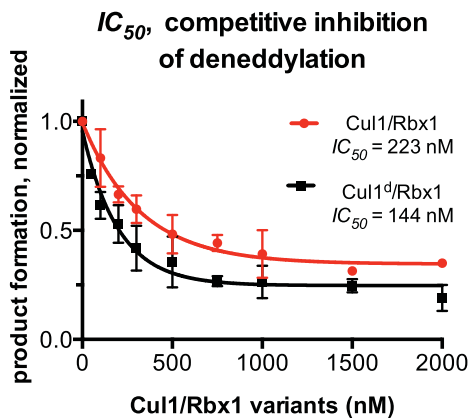


Figure Supplement 2



S2C



S2D

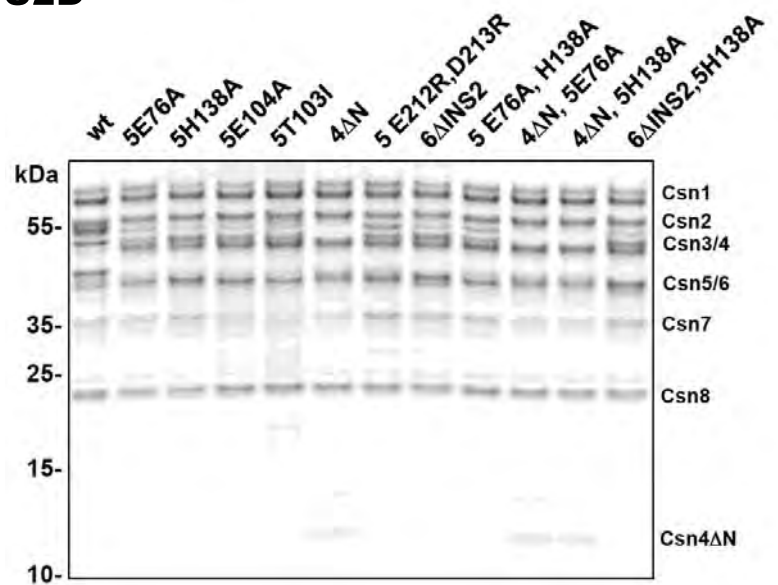
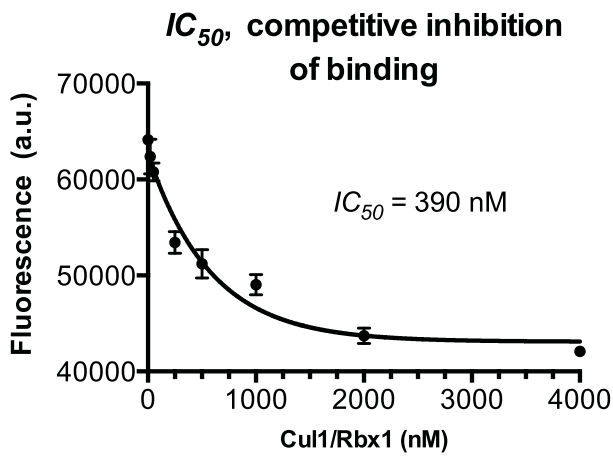
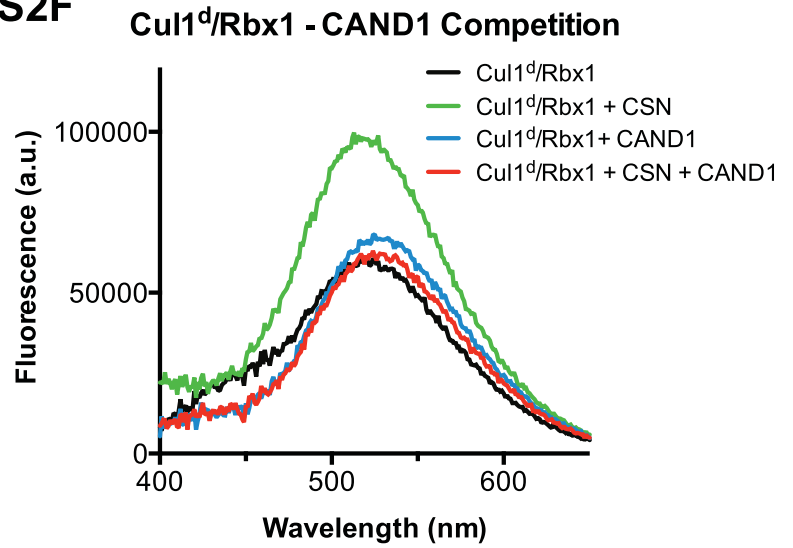


Figure Supplement 2

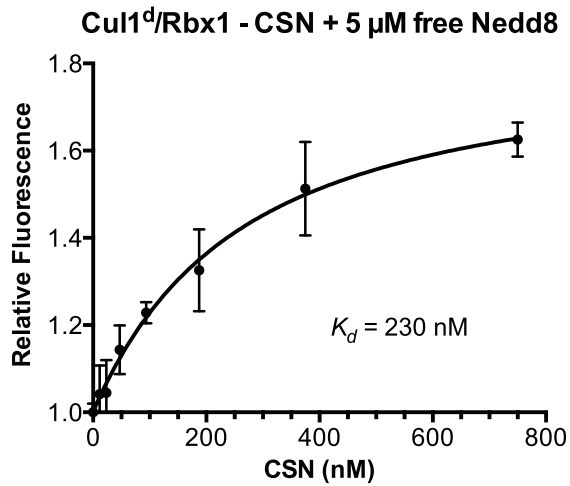
S2E



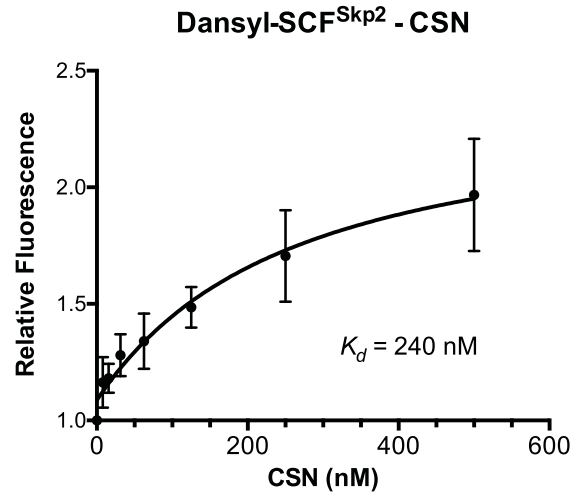
S2F



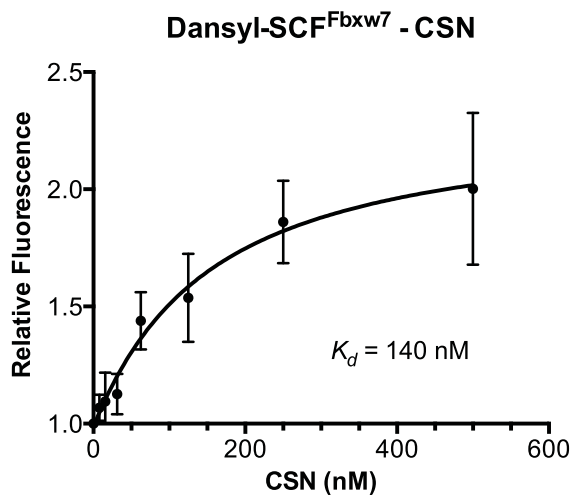
S2G



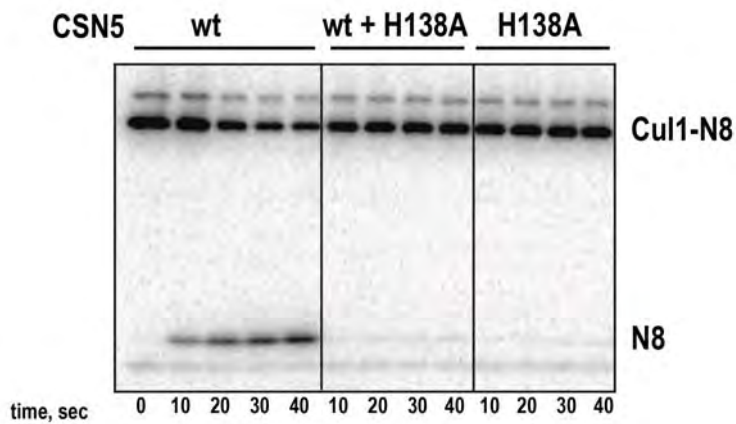
S2H



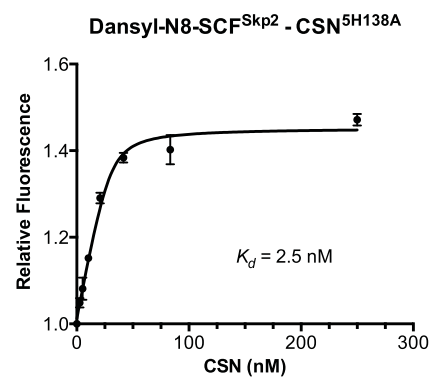
S2I



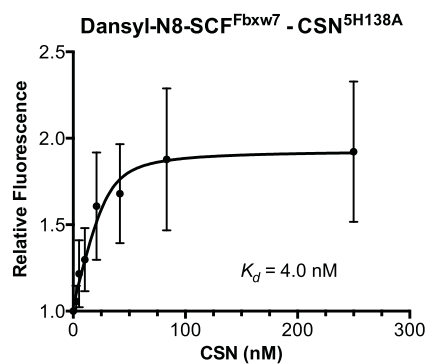
S3A



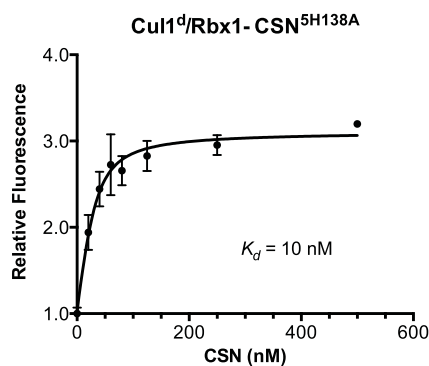
S3B



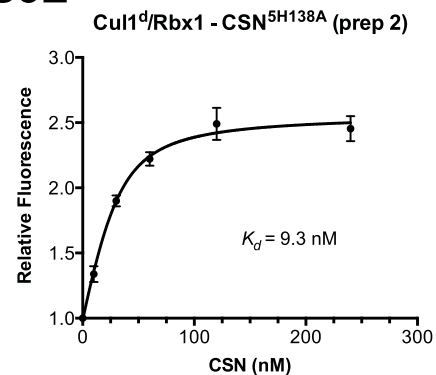
S3C



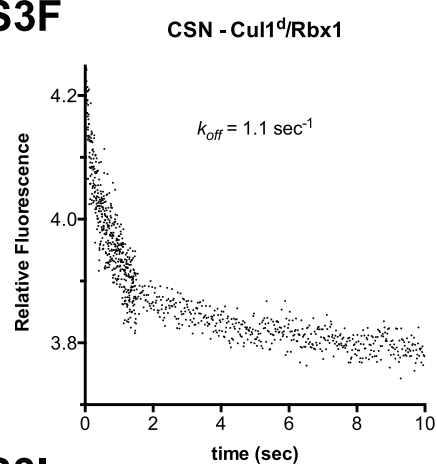
S3D



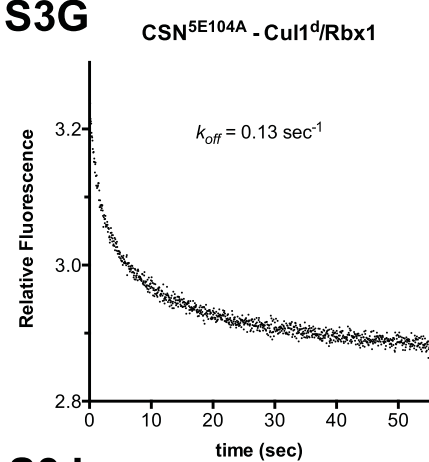
S3E



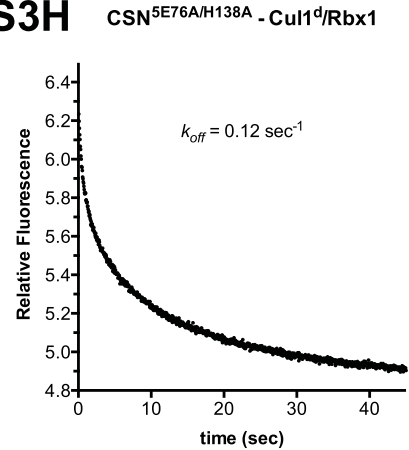
S3F



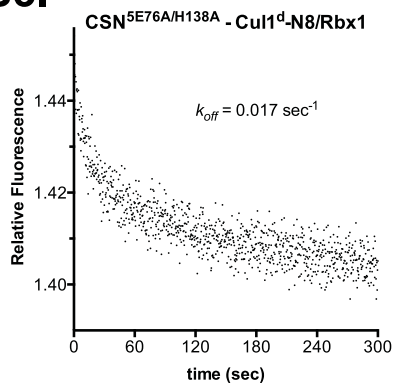
S3G



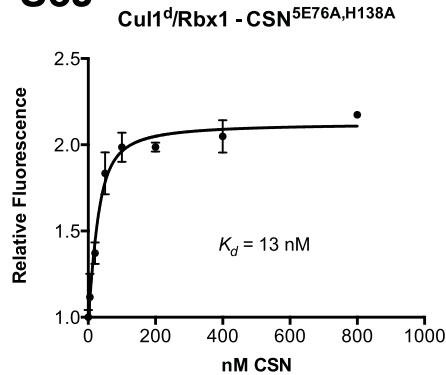
S3H



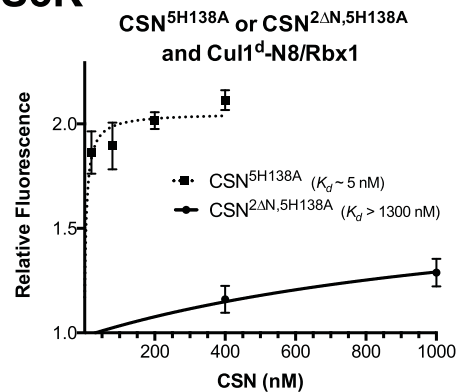
S3I



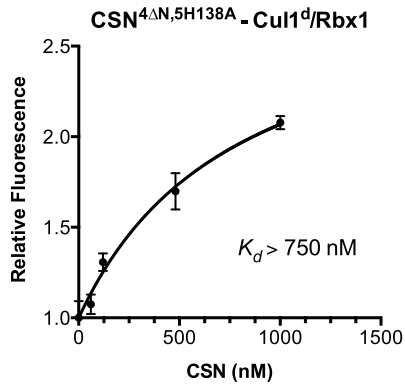
S3J



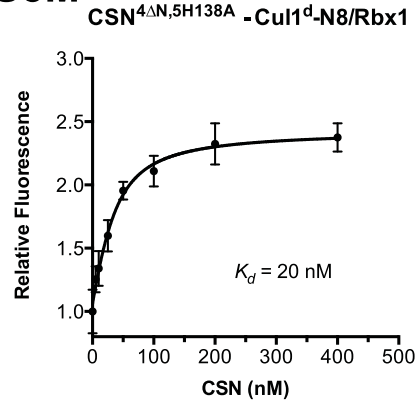
S3K



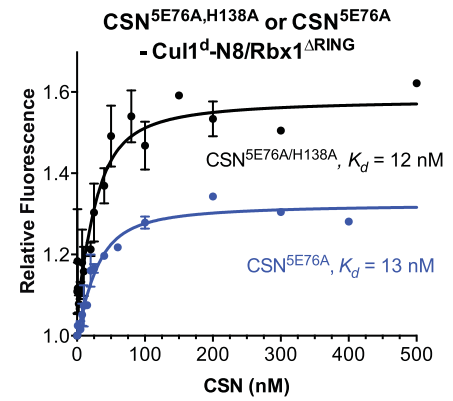
S3L



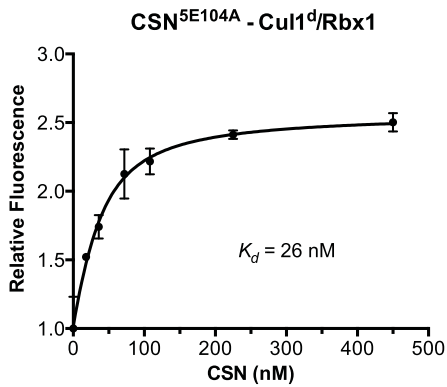
S3M



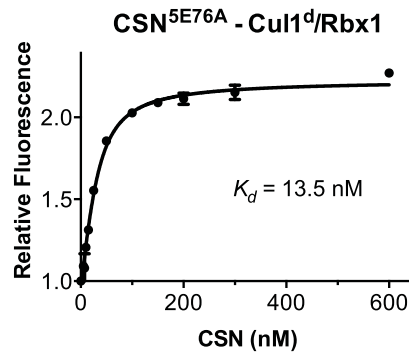
S3N



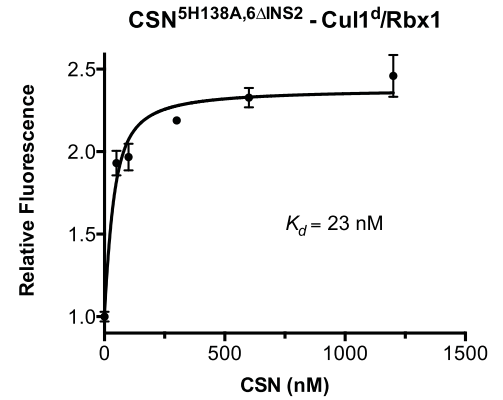
S3O



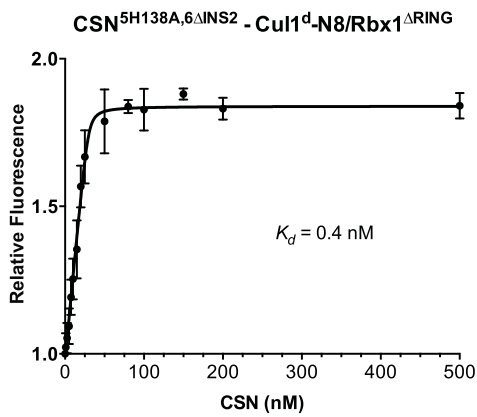
S3P



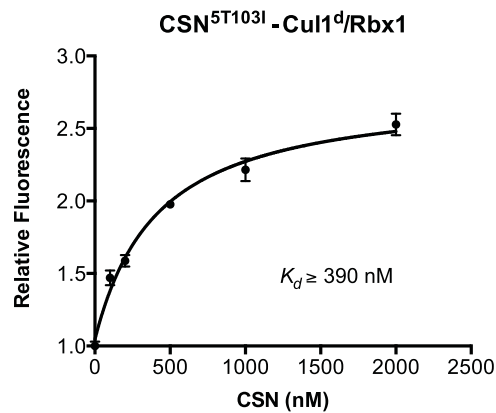
S3Q



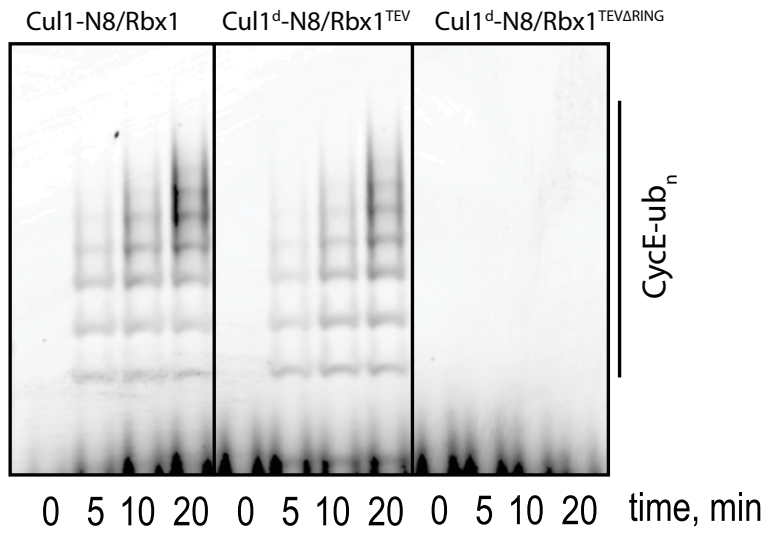
S3R



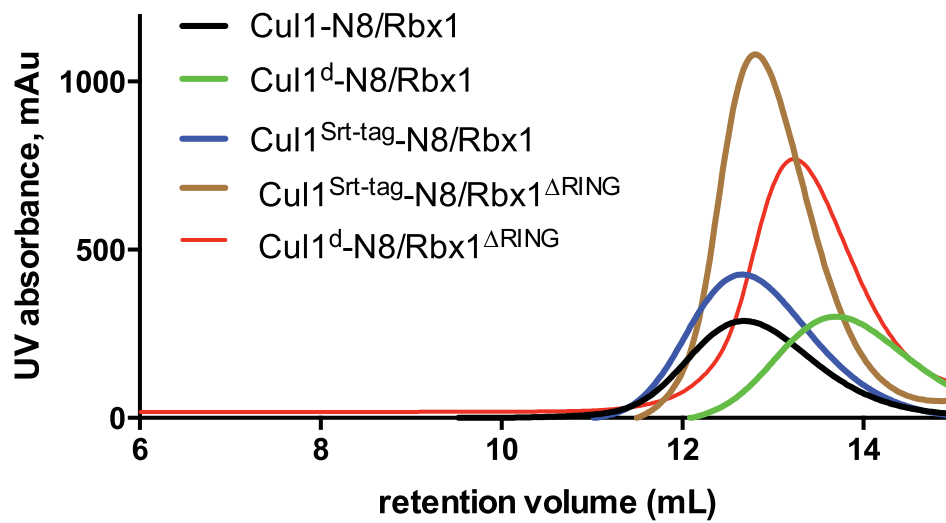
S3S

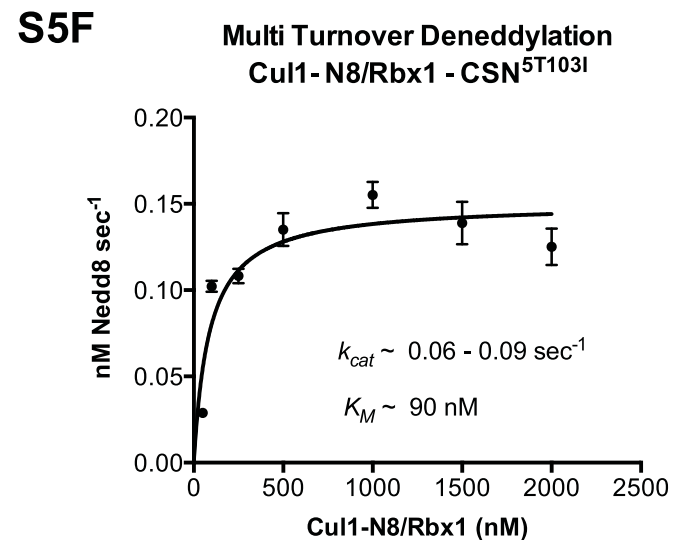
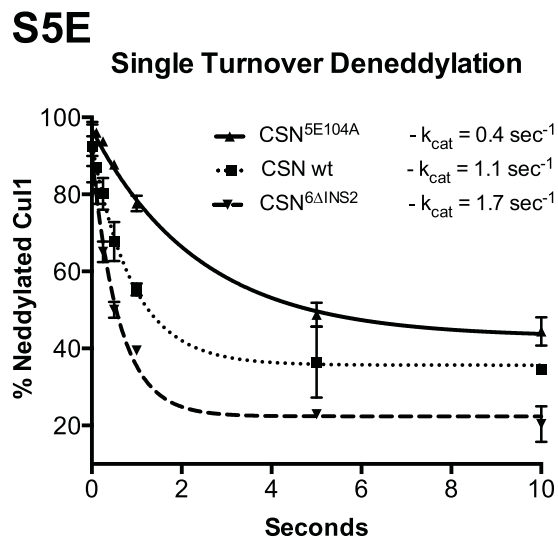
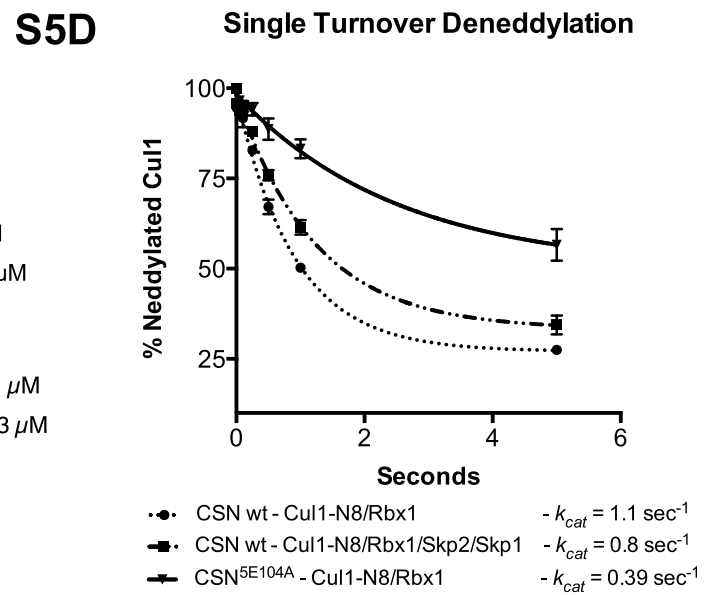
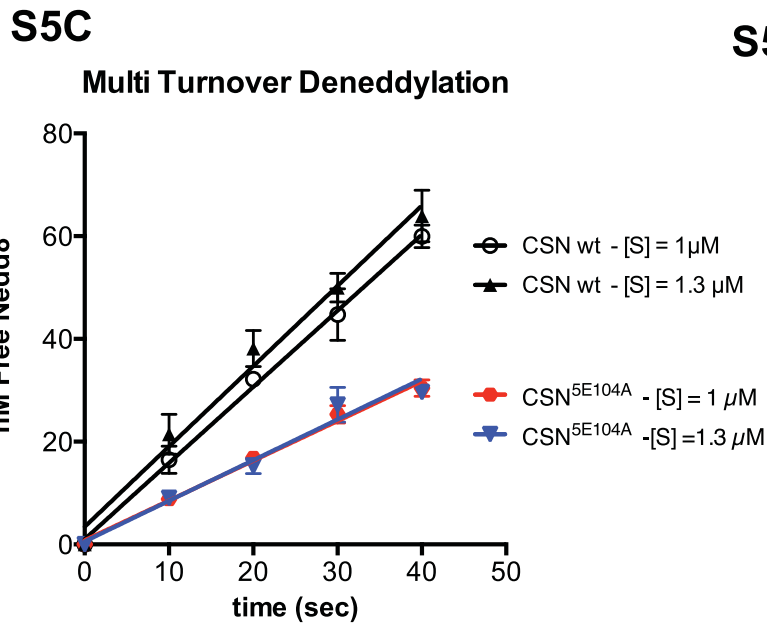
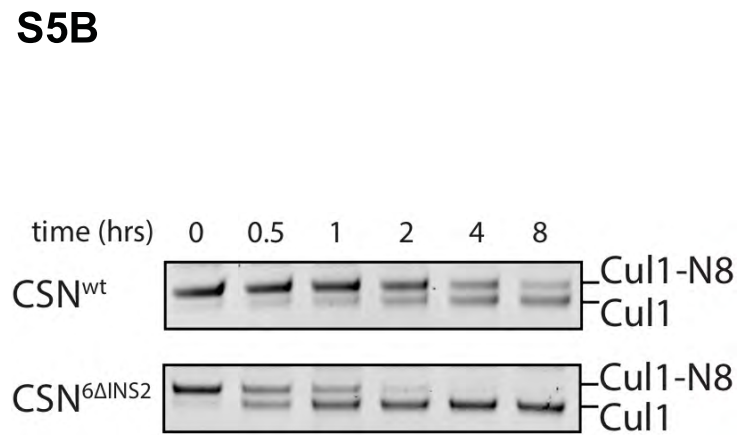
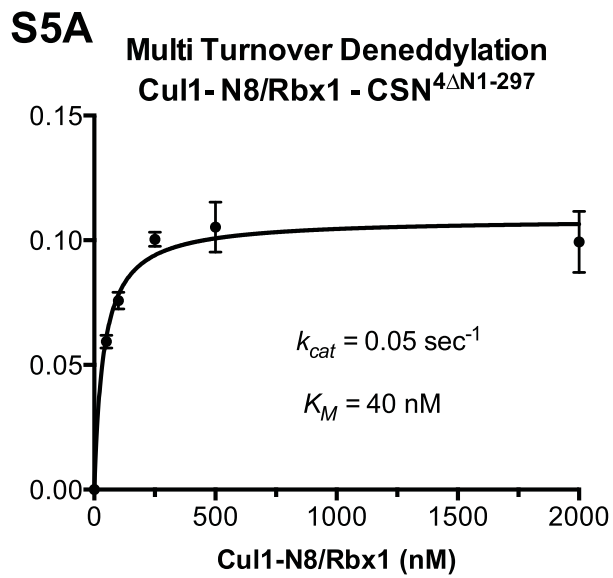


S4A

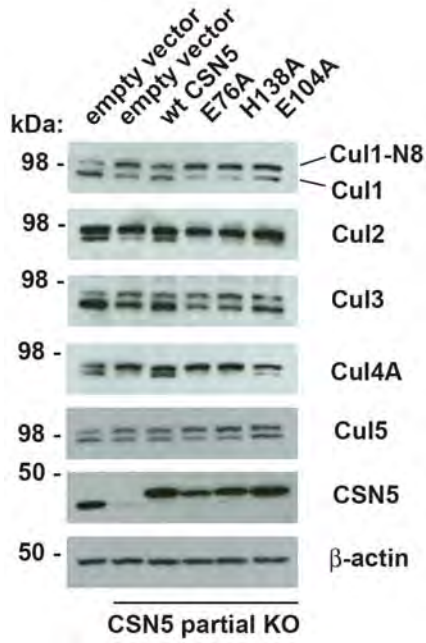


S4B





S6A



S6B

